Formation and growth of co-culture tumour spheroids: new mathematical models and experiments

Ryan J. Murphy[1,*], Gency Gunasingh[2], Nikolas K. Haass[2,†], Matthew J. Simpson[1,†]

[1] *Mathematical Sciences, Queensland University of Technology, Brisbane, Australia*

[2] *Frazer Institute, The University of Queensland, Brisbane, Australia*

Abstract

Co-culture tumour spheroid experiments are routinely performed to investigate cancer progression and test anti-cancer therapies. Therefore, methods to characterise and interpret co-culture spheroid growth are of great interest. However, co-culture spheroid growth is complex. Multiple biological processes occur on overlapping timescales and different cell types within the spheroid may have different characteristics, for example proliferation rate or response to nutrient availability. There is no standard, widely-accepted mathematical model of such complex spatio-temporal growth processes. Typical approaches to analyse these experiments focus on the late-time temporal evolution of spheroid size and overlook early-time spheroid formation, spheroid structure and geometry. Here we make theoretical and practical contributions. We develop a general framework, based on mathematical and statistical modelling, to analyse a series of co-culture experiments. Using a range of different mathematical models we provide new biological insights about spheroid formation, growth, and structure. In addition, we extend a general class of compartment-based monoculture spheroid mathematical models to describe multiple populations and provide mechanistic biological insight. The framework is well-suited to analyse spheroids grown with multiple different cell types and the new class of mathematical models provide opportunities for further mathematical and biological insights.

Key words: heterogeneous population growth, mathematical modelling, parameter estimation, profile likelihood analysis, cancer.

*Corresponding author: r23.murphy@qut.edu.au

†These authors contributed equally.

1 Introduction

Tumour spheroids are a key experimental tool to study cancer progression and to develop cancer therapies [1, 2, 3, 4]. Spheroids also bridge the gap between two-dimensional *in vitro* experiments and three-dimensional *in vivo* experiments. Previously we have developed a framework to characterise the temporal evolution of monoculture spheroid size and structure [5, 6, 7]. Here, we focus on more complicated co-culture tumour spheroid experiments. These experiments are performed with two cell types, melanoma cells and fibroblasts. Each cell type may exhibit different characteristics, for example different proliferation rates or different responses to nutrient availability. Further, within each spheroid multiple biological processes occur on overlapping timescales. Therefore, characterising and interpreting co-culture spheroid growth is challenging. To address this challenge, we develop a general framework based on mathematical and statistical modelling. Throughout we provide novel practical and theoretical contributions. This includes characterising and interpreting co-culture spheroid formation and growth and extending a general class of monoculture compartment-based mathematical models to multiple populations to provide mechanistic biological insight.

Co-culture spheroid experiments are routinely performed to capture some of the complexity of *in situ* tumours, in particular the growth and interactions of multiple cell types [8, 9, 10, 11]. Here, we grow cancer cell line spheroids and incorporate a second cell type, fibroblasts, to enhance spheroid formation and geometry and to explore the impact of the second cell type on growth [10, 11]. To perform our experiments, we place a mixture of melanoma cells and fibroblasts into a well of a cell culture plate, referred to as *seeding*. For all experiments we make a standard choice and seed each spheroid with a total of 5000 cells [5, 6, 13, 14]. The cells then adhere and migrate over a timescale of days to form a three-dimensional compact solid mass, i.e. a spheroid, whose overall size grows in a sigmoidal manner over time (Fig 1A,B) [12, 13]. In the first set of experiments we focus on early time spheroid formation, geometry, and growth. In a second set of experiments we focus on later time temporal evolution of spheroid size and structure. Experimental measurements are obtained by analysing brightfield images captured from above each spheroid, confocal microscopy images of each spheroid's equatorial plane, and three dimensional spheroid renderings from confocal microscopy z-stacks.

To explore early time spheroid formation and subsequent sigmoidal growth, we consider a biphasic mathematical model (Fig 1C) [15]. In each of the two phases, namely formation and growth, the size of the spheroid is described by an ordinary differential equation. This allows us to estimate spheroid formation time and extends traditional analysis that overlook formation [16, 17, 18]. Early time growth dynamics are reasonably described with a linear model (Fig 1D). We connect each mathematical model to experimental data using statistical modelling. Specifically, we use profile likelihood analysis for parameter estimation, to form approximate confidence intervals, and to assess if parameters are *practically identifiable* [6, 15, 18, 19, 20, 21]. A parameter is practically identifiable if it can be uniquely identified given a finite set of noisy experimental data. This is in contrast to

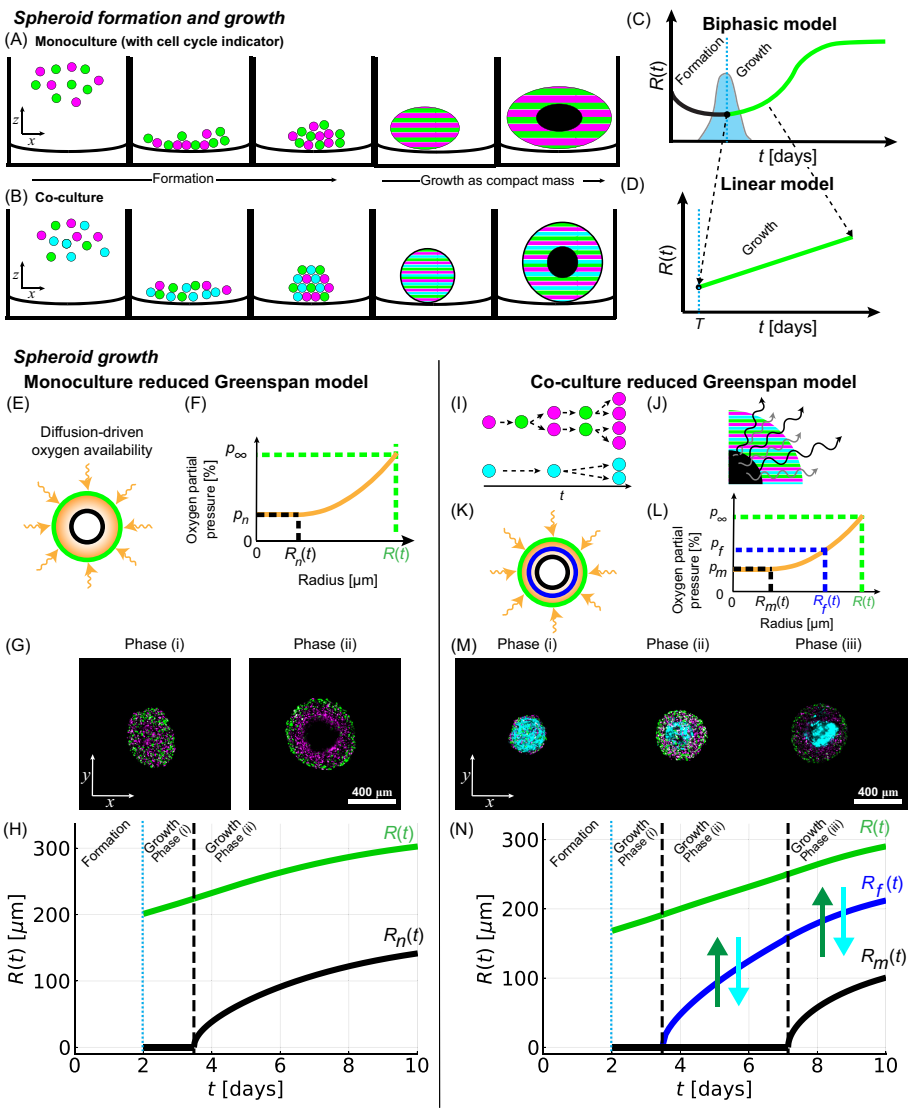

Figure 1: Characterising co-culture tumour spheroid growth using mechanistic mathematical modelling. (A-B) Spheroid formation and growth schematics. Cells placed into a well adhere and migrate to form a compact solid mass, i.e. a spheroid, which grows. Dots represent cells, striped shading represents regions of multiple cell types, and black circles represent necrotic core. (A) Monoculture with cell cycle indicator (FUCCI). Throughout, colours represent FUCCI signals observed in experimental images, e.g. (G): cells in gap 1 (G1) phase fluoresce red, shown in magenta for clarity; and cells in synthesis, gap 2, and mitotic (S/G2/M) phases fluoresce green (B) Co-culture with two cell types: one cell type (melanoma) with cell cycle indicator (magenta, green) and one cell type (fibroblasts) without (cyan). (C) Schematic for biphasic model that captures spheroid formation (black), spheroid growth (green), and from which we form a profile to estimate spheroid formation time (cyan shaded). Cyan dashed line indicates best estimate of time at which spheroid forms. (D) Early time growth approximated with a linear model. (E-H) Monoculture reduced Greenspan mathematical model for spheroid growth. (E,F) Oxygen diffuses within the spheroid and is consumed by living cells which gives rise to gradient in the oxygen partial pressure within the spheroid. Cells are assumed to die below an oxygen partial pressure threshold p_n [%]. (G) Representative confocal microscopy images of the equatorial plane of a M100:F0 spheroid. (H) Simulation of the monoculture reduced Greenspan model. (I-N) Co-culture reduced Greenspan model for spheroid growth. (I) Schematic for heterogeneity in the proliferation rates of the two cell types. (J) Schematic for heterogeneity in the loss rates from the necrotic core for the two cell types. (K,L) Oxygen diffuses within the spheroid and is consumed by living cells which gives rise to gradient in the oxygen partial pressure within the spheroid. Melanoma cells and fibroblasts are assumed to die below an oxygen partial pressure thresholds p_{m} [%] and p_{f} [%], respectively. (M) Representative confocal microscopy images of the equatorial plane of a M50:F50 spheroid. (N) Simulation of a co-culture reduced Greenspan model with two oxygen partial pressure thresholds and additional cell migration (green/blue arrows for melanoma/fibroblasts, respectively).

structural identifiability studies that assess whether parameters can be uniquely identified given a set of continuous noise-free observations [21].

In a second set of experiments we focus on the temporal evolution of spheroid structure. In monoculture spheroid experiments, growth after formation can be characterised by two phases. First, at early times each cell within the spheroid is able to proliferate and the spheroid grows exponentially. Second, at later times a necrotic core forms, thought to be due to lack of oxygen (Fig 1E,F) [7]. The spheroid then grows to a limiting size and structure where proliferation at the periphery is thought to balance loss from the necrotic core (Fig 1H) [5, 6, 7, 22]. To visualise living and necrotic regions within each spheroid, we use fluorescent ubiquitination-based cell cycle indicator (FUCCI) transduced melanoma cell lines (Fig 1G) [14, 23]. The presence of FUCCI signals indicate living cells and a large central region that lacks FUCCI signals indicates a necrotic core (Fig 1G). We have previously shown that the seminal Greenspan mathematical model describes monoculture spheroid growth remarkably well [5, 6, 7, 22] (Fig 1E-H). Here, we quantitatively directly connect Greenspan's model to co-culture spheroid data for the first time. Alternative mathematical models are reviewed in [24, 25, 26, 27]. For example, individual-based models that prescribe rules that govern the dynamics of each cell [28, 29, 30] or continuum models in the form of partial differential equations [31, 32]. However, these models typically contain parameters that are challenging to estimate using data collected in this study. Further, the biological interpretation of parameters in such models can be unclear.

When we take a purely experimental approach quantitative differences and similarities in co-culture spheroid growth, and the mechanisms giving rise to these similarities and differences, are unclear. For example, how does the addition of a second cell type influence spheroid growth and structure? Further, in our experiments we find that fibroblasts are located throughout the spheroid at early times but are present only in the central region of the spheroid at later times (Fig 1M) [10, 33]. The biological mechanisms driving this process are unclear. For example, it could be that melanoma cells outcompete fibroblasts at the periphery or it could be that melanoma cells migrate to the periphery or fibroblasts actively migrate the centre of the spheroid. To characterise co-culture spheroid growth, we require a framework to capture, test, and explore such observations and hypotheses.

Greenspan's compartment-based mathematical model has played an important role in developing our understanding of monoculture spheroid growth. Each compartment corresponds to a region in the spheroid, for example the periphery or the necrotic core. The model is derived by coupling conservation of volume arguments with geometric constraints that define the boundary of each region. In general, geometric constraints in compartment-based spheroid models may be prescribed [18] or derived by considering additional biological mechanisms. In Greenspan's model the geometric constraints arise by considering oxygen diffusion and consumption [22]. Many other compartment-based models have been developed to analyse monoculture spheroid growth. For example, the Burton model [34]; studies reviewed and discussed in [24, 25, 27, 35] including works by Deakin

[36], McElwain and Ponzo [37], McElwain and Morris [38], Adam [39, 40, 41], Adam and Maggelakis [42, 43], Maggelaskis and Adam [44], Landry [45], Byrne et al. [46, 47]; and more recently the radial-death model [18]. However, to the best of our knowledge, such compartment-based models have been restricted to one cell type. In this study, we extend these compartment-based spheroid models subject to general geometric constraints and develop a general model with I populations and J compartments. Then, using this general model, we efficiently and systematically develop multiple two population extensions of Greenspan's model. Exploring these new models reveals biological mechanisms that can describe the co-culture experimental data and those that cannot.

2 Experimental methods

We perform two co-culture experiments. Both experiments are performed for ten days with two human melanoma cell lines (WM983B, 1205Lu) and human primary fibroblasts (QF1696) at five different initial compositions (M100:F0, M75:F25, M50:F50, M25:F75, M0:F100, where Mx:Fy is the initial proportion, measured as a percentage, of melanoma cells x [%] and fibroblasts $y = 100 - x$ [%]). The first experiment focuses on brightfield images captured from above each spheroid of spheroid formation and growth. The second experiment focuses on growth characteristics after formation, specifically the temporal evolution of spheroid size, internal structure, and geometry. For the second experiment we analyse the equatorial plane of each spheroid using confocal microscopy and also capture representative 3D z-stack images of spheroid geometry. The melanoma cell lines were previously transduced with fluorescent ubiquitination-based cell cycle indicator (FUCCI) constructs [14]. Using FUCCI-transduced cell lines allows us to visualise the cell-cycle status of each melanoma cell and identify the necrotic core of each spheroid. Fibroblasts are identified using CellTracker™ Deep Red dye. The fibroblast marker stains the entire cell whereas the FUCCI signal is only present at the cell nucleus. In the following we detail the experimental methods: cell culture; spheroid generation, culture, and experiments; imaging; and image processing.

2.1 Cell culture

The methods for cell culture are identical to that previously described in our previous tumour spheroid studies [6, 7]. For clarity we outline the method here. The human melanoma cell lines WM983B, and 1205Lu were provided by Professor Meenhard Herlyn, The Wistar Institute, Philadelphia, PA, [48], previously genotypically characterised [14, 49, 50, 51], grown as described in [13], and previously authenticated by short tandem repeat fingerprinting (QIMR Berghofer Medical Research Institute, Herston, Australia). Both melanoma cell lines were previously transduced with fluorescent ubiquitination-based cell cycle indicator (FUCCI) constructs as described in [13, 14]. Human primary fibroblast QF1696 were a gift from Associate Professor Rick Sturm (Frazer Institute, University of Queensland) [52].

2.2 Spheroid generation, culture, and experiments.

Spheroids were generated in 96-well cell culture flat-bottomed plates (3599, Corning), with a total seeding density of 5000 total cells/well, using 50 µL total/well non-adherent 1.5% agarose to promote formation of a single spheroid per well [13]. For the second experiment focusing on spheroid structure, fibroblasts were stained with CellTracker™ Deep Red dye as per manufacturer's instructions prior to seeding. For both experiments melanoma cells and fibroblasts were mixed at seeding to the desired percentages: M100:F0, M75:F25, M50:F50, M25:F75, M0:F100, where Mx:Fy is the initial proportion, measured as a percentage, of melanoma cells x [%] and fibroblasts $y = 100 - x$ [%]. For all experiments 50% of the medium in each well was replaced with fresh medium (200 µL total/well) every 3-4 days for the duration of the experiment. Incubation and culture conditions were as described in §2.1.

2.3 Imaging and image processing to capture overall size

In the first experiment to estimate the radius of each spheroid at time t, $R(t)$, we use the IncuCyte S3 live cell imaging system (Sartorius, Goettingen, Germany). For each melanoma cell type, we seed sixteen spheroids for the M100:F0 condition, and eight spheroids for the M75:F25, M50:F50, M25:F75, and M0:F100 conditions into a plate (§2.2). The plate is placed inside the IncuCyte S3 live cell imaging incubator (37 °C, 5% CO_2) immediately after seeding. IncuCyte S3 settings were chosen to image hourly for the duration of the experiment with the 10× objective. Brightfield images captured from above each spheroid with the IncuCyte S3 are processed using the accompanying IncuCyte 2020C Rev1 software (spheroid analysis type, brightfield image channel, largest object area, `hole fill` $= 1 \times 10^4$ µm^2). Area masks were visually compared with the IncuCyte brightfield images to confirm accuracy (Figure 2). For each spheroid the mask area, $A(t)$, at time t was converted to an equivalent spheroid radius measurement $R(t) = \sqrt{A(t)/\pi}$. These measurements are used for analysis. At later times cellular debris can form outside of the main spheroid mass, but this is limited and so it is not included in the analysis. Some measurements could not be obtained, primarily due to blurring of the automated imaging.

2.4 Imaging to capture spheroid structure using confocal microscopy

To capture spheroid structure as part of the second experiment we use confocal microscopy and follow the experimental procedure described in [55]. Spheroids maintained in the incubator were harvested, fixed with 4% paraformaldehyde (PFA), and stored in phosphate buffered saline solution, sodium azide (0.02%), Tween-20 (0.1%), and DAPI (1:2500) at 4 °C, on days 2, 3, 6, 8 and 10 after seeding. Fixed spheroids were set in place using low melting 2% agarose and optically cleared in 500 µL total/well high refractive index mounting solution (Quadrol 9 % wt/wt, Urea 22 % wt/wt, Sucrose 44 % wt/wt, Triton X-100 0.1 % wt/wt, water) for 2 days in a 24-well glass bottom plate (Cellvis, P24-1.5H-N) before imaging to ensure accurate measurements. Images were then captured

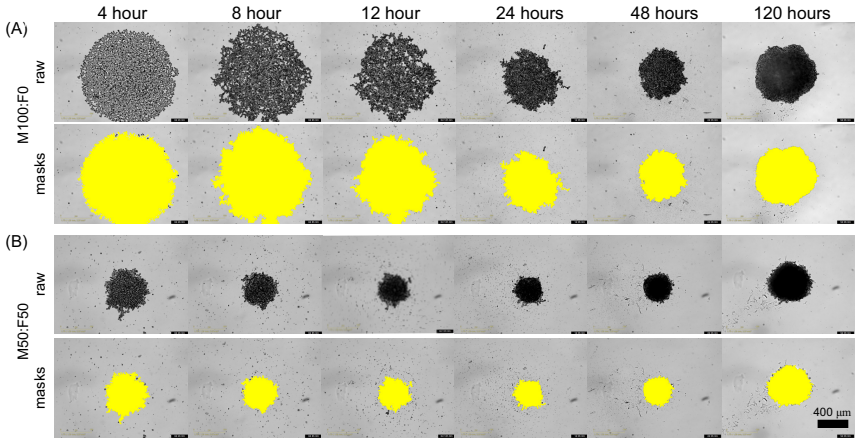

Figure 2: Brightfield images processing for spheroid formation and growth. Results shown for (A) M100:F0 and (B) M50:F50 1205Lu co-culture spheroids. In (A,B) top rows show raw images and bottom rows masks (yellow). Top and bottom rows show the same spheroids. Scale bar is 400 µm.

using an Olympus FV3000 confocal microscope with the 10× objective focused on the equatorial plane of each spheroid.

2.5 Image processing for confocal images

We analyse confocal images using standard tools in a CellProfiler pipeline [12, 53] to estimate the spheroid radius, $R(t)$, and necrotic core radius, $R_{\mathrm{n}}(t)$. Methods are similar to [54]. In brief, we use four channels from the raw confocal microscopy images. These channels correspond to: (i) DAPI, a stain of the nucleus of each melanoma and fibroblast cell; (ii) FUCCI green, which identifies melanoma cells in S/G2/M phases of the cell cycle (shown in green); (iii) FUCCI red, which identifies melanoma cells in G1 phase of the cell cycle (shown in magenta), and (iv) a fibroblast marker, which identifies fibroblast cells (shown in cyan). To estimate the area covered by each spheroid we use the DAPI signals; binarise, using the `threshold` function; fill gaps between cells, using the `dilate` and `erode` pixels functions with a disk of the same magnitude and then the `RemoveHoles` function; and finally use the `IdentifyPrimaryObjects` function. To estimate the area of the necrotic core we merge the signals from the FUCCI red and FUCCI green channels using the `GrayToColor` function; convert the merged signals to a grayscale image, using the `ColorToGray` function; binarise the image, using the `threshold` function; remove gaps between cells in the periphery region, using the `dilate`, `RemoveHoles`, and `erode` functions; invert the binary image, using the `ImageMath` function; and then use the `IdentifyPrimaryObjects` function with an upper bound on the maximum size expected to capture the necrotic core rather than the area external to the spheroid. Area masks for the spheroid and necrotic core were visually compared to confirm accuracy (§S1.2). For each spheroid, the spheroid mask area, $A(t)$, and the necrotic core mask area, $A_{\mathrm{n}}(t)$, at time t were converted to equivalent radii measurements, $R(t) = \sqrt{A(t)/\pi}$ and $R_{\mathrm{n}}(t) = \sqrt{A_{\mathrm{n}}(t)/\pi}$. These measurements are used for analysis.

3 Mathematical models to analyse spheroid formation and size

3.1 Spheroid formation and size

We analyse three-dimensional spheroid formation using the biphasic model introduced in [15] (Fig 1C). In the first phase, cells that are placed in the well of a tissue culture plate migrate and adhere to form a compact solid mass (Fig 1A,B). The projected area covered by cells, as viewed from above, shrinks until the spheroid forms, for example compare the yellow masks from 4 hours to 48 hours in Figure 2. In the second phase, the spheroid grows as a three-dimensional compact mass. We describe each phase using a logistic-type model with distinct parameters,

$$\frac{\mathrm{d}R(t)}{\mathrm{d}t} = \begin{cases} r_1 R(t)\left(1 - \dfrac{R(t)}{\mathcal{R}_1}\right), & 0 \leq t \leq T, \\ r_2 R(t)\left(1 - \dfrac{R(t)}{\mathcal{R}_2}\right), & t > T, \end{cases} \tag{1}$$

where $R(t)$ [µm] describes the equivalent radius of the projected area covered by cells and T [days] is the formation time. In the second phase, $t > T$ [days], $R(t)$ is equivalent to the radius of the spheroid. Further, r_1 [day^{-1}] is associated with the rate at which the spheroid forms; $\mathcal{R}_1$ [µm] is the limiting radius of the spheroid in the first phase; r_2 [day^{-1}] is the growth rate of the spheroid as a compact mass; and $\mathcal{R}_2$ [µm] is the long-time maximum spheroid radius. The initial spheroid size, $R(0)$ [µm], satisfies $R(0) > \mathcal{R}_1$ to observe shrinking in the first phase. Hence, $R(t) > \mathcal{R}_1$ for $0 \leq t \leq T$. In the second phase, $t > T$, $R(t) \to \mathcal{R}_2$ as $t \to \infty$. This model is characterised by six parameters $\theta = (R(0), r_1, r_2, \mathcal{R}_1, \mathcal{R}_2, T)$ that we will estimate from our experimental data.

3.2 Spheroid size

Focusing on three-dimensional spheroid growth, we do not observe spheroids reaching a long-time maximum size during this experiment. Therefore, we simplify our analysis and approximate early time exponential growth dynamics in the second phase of the model presented in Eq. (1) with a linear model (Fig 1D, Supplementary S2.1), i.e. $\exp(\lambda t) = 1 + \lambda t + \mathcal{O}((\lambda t)^2)$ when λt is small [57], to give

$$R(t) = R(T)(1 + \lambda t). \tag{2}$$

where $R(t)$ [µm] is the radius of the spheroid, $R(T)$ [µm] is the radius of the spheroid at the end of formation that we treat as a constant parameter, and λ [day^{-1}] is the growth rate. This model is characterised by two parameters $\theta = (R(T), \lambda)$ that we will estimate from our experimental data.

4 Mathematical models to analyse spheroid structure

In this section we present a general compartment-based spheroid model with I populations and J compartments that is subject to geometrical constraints. Geometrical constraints, for example to define the size of proliferating region, may be prescribed [18] or arise by considering additional biological mechanisms, for example oxygen, nutrient, or waste mechanisms [22]. In this framework, a population could refer to a cell type, for example melanoma or fibroblasts, or the state of the cell, for example living or dead. Here, when we refer to a population we intend the former, but the framework is general and either interpretation can be considered. This general model extends previous compartment-based models that have been restricted to one population, for example Greenspan's seminal model [22] and the radial-death model [18] (§S4.1). We derive the general model from conservation of volume arguments that incorporate geometric constraints and biological mechanisms, for example cell proliferation, cell death, and cell migration. Motivated by our new experimental data of co-culture spheroid growth, we then describe simplifications of the general model to explore a reduced version of Greenspan's monoculture model and four new co-culture models.

4.1 General model

We assume that the tumour spheroid is a compact mass maintained by surface tension or cell-cell adhesion, however the details of such mechanisms are not explicitly modelled nor crucial to model description [22]. We further assume that each compartment within the tumour spheroid is spherically symmetric, populations are well-mixed within each compartment, and all compartments are concentric. In Figure 3 we present a schematic of the general model with I populations and J compartments. We let $V_i^{(j)}(t)$ denote the volume of population i in compartment j at time t for $i = 1, 2, \ldots, I$ and $j = 1, 2, \ldots, J$; $V^{(j)}(t)$ denote the total volume of compartment j for $j = 1, 2, \ldots, J$; $V(t)$ denote the total volume of the spheroid; $R_0(t)$ denote the radius of the spheroid, i.e. $R_0(t) = R(t)$; and $R_j(t)$ denote the boundary between internal compartments j and $j + 1$ for $j = 1, 2, \ldots, J - 1$. Therefore, compartment j denotes the region $R_j(t) < r < R_{j-1}(t)$ for $j = 1, 2, \ldots, J - 1$ and compartment J denotes the region $0 < r < R_{J-1}(t)$. The only independent variables are time, t [days], and radial position, r [µm]. Geometrical constraints, for example to define the size of proliferating region, may be prescribed [18] or arise by considering additional biological mechanisms, for example oxygen, nutrient, or waste mechanisms [22].

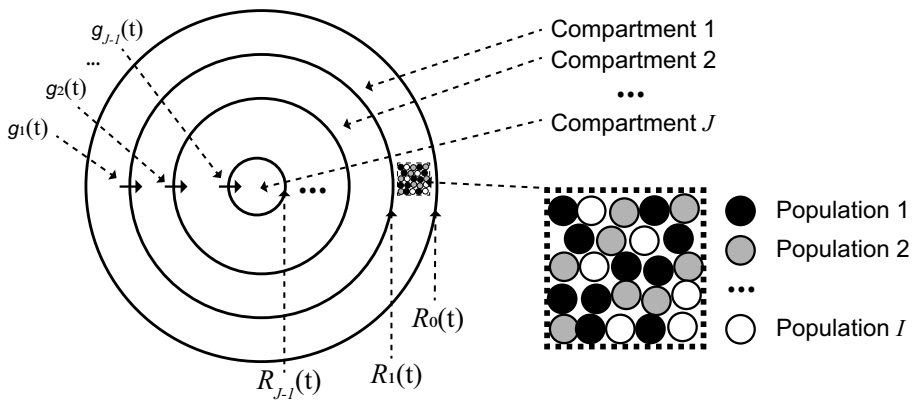

Figure 3: Schematic for general compartment-based tumour spheroid model with I populations and J compartments.

A general conservation of volume statement for I populations and J compartments, subject to geometrical constraints (Eqs (3.6), is

$$\frac{\mathrm{d}V_i^{(j)}(t)}{\mathrm{d}t} = \begin{cases} \underbrace{f_{V_i^{(j)}}(R(t);p)}_{\text{source, sink, reaction, migration}} - \underbrace{g^{(j)}(R(t);p)}_{\substack{\text{migration due to}\\ \text{geometric constraint}}} \underbrace{g_i^{(j)}(R(t);p)}_{\text{proportion}\in[0,1]}, & j=1,\ i=1,2,\ldots,I, \\ f_{V_i^{(j)}}(R(t);p) + g^{(j-1)}(R(t);p)g_i^{(j-1)}(R(t);p) - g^{(j)}(R(t);p)g_i^{(j)}(R(t);p), & \\ \qquad\qquad\qquad\qquad\qquad\qquad\qquad\qquad\qquad\qquad j=1,\ldots,J-1,\ i=1,2,\ldots,I, & \\ f_{V_i^{(j)}}(R(t);p) + g^{(j-1)}(R(t);p)g_i^{(j-1)}(R(t);p), \quad j=J,\ i=1,2,\ldots,I, & \end{cases} \tag{3.1}$$

$$\sum_{i=1}^{I} g_i^{(j)}(t) = 1, \quad j=1,2,\ldots,J, \text{ with } g_i^{(j)}(t) \geq 0, \quad \text{for} \quad i=1,2,\ldots,I,\ j=1,2,\ldots,J-1, \tag{3.2}$$

$$V^{(j)}(t) = \sum_{i=1}^{I} V_i^{(j)}(t), \quad j=1,2,\ldots,J, \tag{3.3}$$

$$V(t) = \sum_{j=1}^{J} V^{(j)}(t), \tag{3.4}$$

$$V^{(j)}(t) = \begin{cases} \frac{4\pi}{3}\left(R_{j-1}(t)^3 - R_j(t)^3\right), & j=1,2,\ldots,J-1, \\ \frac{4\pi}{3}R_j(t)^3, & j=J \end{cases} \tag{3.5}$$

$$R_j(t) = \underbrace{f_j(R(t);p)}_{\text{geometric constraint}}, \quad j=1,2,\ldots.J-1. \tag{3.6}$$

To solve Eq (3.1)-(3.6) we prescribe the following functions: (i) $f_{V_i^{(j)}}(R(t);p)$ for $i=1,2,\ldots,I$ and $j=1,2,\ldots,J$ that describe sources, sinks, reactions, and/or migration; and (ii) $f_j(R(t);p)$ for $j=1,2,\ldots,J-1$ that describe geometric constraints. These prescribed functions depend on $R(t)$ and a vector of model parameters, p, that are also to be prescribed. As we assume a well-mixed population we set the migration of population i across the boundary $R_j(t)$ due to the geometric constraint to be proportional to the volume fraction of population i in compartment j, i.e. we set $g_i^{(j)}(R(t);p) = V_i^{(j)}(t)/V^{(j)}(t)$ for $i=1,2,\ldots,I$ and $j=1,2,\ldots,J-1$. This choice of $g_i^{(j)}(R(t);p)$

satisfies Eq (3.2) which ensures that the total migration across the boundary $R_j(t)$ due to the geometric constraint is $g^{(j)}(t)$. Further, enforcing that each $g_i^{(j)}(R(t);p)$ is non-negative in Eq (3.2) ensures that all migration due to the geometric constraint is in the same direction. This does not mean that all cell migration is in the same direction as additional cell migration may be prescribed in the functions $f_{V_i^{(j)}}(R(t);p)$. Eqs (3.3)-(3.4) ensure there are no voids within the spheroid. Eqs (3.5) arise from the assumption of spherically symmetry, namely that the volume of a sphere of radius r is $4\pi r^3/3$. Eqs (3.1), (3.3)-(3.6) form a system of $IJ+3J$ equations for $IJ+3J$ unknowns ($V_i^{(j)}(t)$ for $i=1,2,\ldots,I$ and $j=1,2,\ldots,J$; $g^{(j)}(t)$ for $j=1,2,\ldots,J-1$; $V^{(j)}(t)$ for $j=1,2,\ldots,J$; $V(t)$; and R_j for $j=0,1,2,\ldots,J-1$).

In Supplementary Material S2.2, we transform Eq (3) to the following system of $IJ+2J-1$ equations for $IJ+2J-1$ unknowns ($V_i^{(j)}(t)$ for $i=1,2,\ldots,I$ and $j=1,2,\ldots,J$; $g^{(j)}(t)$ for $j=1,2,\ldots,J-1$; and R_j for $j=0,1,2,\ldots,J-1$) that we solve numerically (Supplementary S3)

$$\frac{\mathrm{d}V_i^{(j)}(t)}{\mathrm{d}t} = \begin{cases} f_{V_i^{(j)}}(R(t);p) - g^{(j)}(R(t);p)g_i^{(j)}(R(t);p) & j=1,\ i=1,2,\ldots,I, \\ f_{V_i^{(j)}}(R(t);p) + g^{(j-1)}(R(t);p)g_i^{(j-1)}(R(t);p) - g^{(j)}(R(t);p)g_i^{(j)}(R(t);p), & \\ & j=1,\ldots,J-1,\ i=1,2,\ldots,I, \\ f_{V_i^{(j)}}(R(t);p) + g^{(j-1)}(R(t);p)g_i^{(j-1)}(R(t);p), & j=J, \end{cases} \tag{4.1}$$

$$\frac{\mathrm{d}R_0(t)}{\mathrm{d}t} = \frac{1}{4\pi R_0(t)^2}\sum_{j=1}^{J}\sum_{i=1}^{I} f_{V_i^{(j)}}(R(t);p)\,, \tag{4.2}$$

$$g^{(j)}(R(t);p) = \left(\sum_{k=1}^{j}\sum_{i=1}^{I} f_{V_i^{(k)}}(R(t);p)\right) - 4\pi\frac{\mathrm{d}R_0(t)}{\mathrm{d}t}\left(R_0(t)^2 - R_j(t)^2\frac{\mathrm{d}R_j(t)}{\mathrm{d}R_0(t)}\right), \quad j=1,2,\ldots,J-1, \tag{4.3}$$

$$R_j(t) = \underbrace{f_j(R(t);p)\,,}_{\text{geometric constraint}} \qquad j=1,2,\ldots.J-1, \tag{4.4}$$

where it is assumed that an expression for $\mathrm{d}R_j(t)/\mathrm{d}R_0(t)$ in terms of $R_0(t)$ for $j=1,2,\ldots,J-1$ can be derived from the prescribed functions in Eq (4.4). Given $V_i^{(j)}(t)$ for $i=1,2,\ldots,I$ and $j=1,2,\ldots,J$ from the solution of Eq (4) we obtain $V^{(j)}(t)$ for $j=1,2,\ldots,J$ and $V(t)$ using Eqs (3.3)-(3.4), respectively. Therefore, this method solves the full general model. Motivated by our new experimental data, we will now describe four simplifications of our general model so that it applies to our particular experimental conditions.

4.2 Monoculture reduced Greenspan model

The monoculture reduced Greenspan model considers one population and two compartments ($I = 1$, $J = 2$), captures key characteristics of Greenspan's model, and describes growth with two phases. In phase (i) all cells within the spheroid can proliferate and the spheroid grows exponentially. In phase (ii) the spheroid is composed of two compartments: compartment one which is a proliferating region at the periphery, $R_1(t) < r < R(t)$, and compartment two which is the necrotic core, $0 \leq r \leq R_1(t)$. At later times proliferation at the periphery balances mass loss from the necrotic core resulting in a limiting spheroid structure [5, 6, 22]. For consistency with the literature we write $R_1(t)$ as $R_{\mathrm{n}}(t)$ and $R_0(t)$ as $R(t)$ [6, 7, 22]. We define $R_{\mathrm{n}}(t)$ through a geometric constraint obtained by considering additional biological mechanisms, specifically oxygen diffusion and consumption [7].

We assume that in the proliferating region the rate at which cell volume is produced by mitosis per unit volume of living cells is s [day^{-1}]. In the necrotic region we assume that the rate at which cell volume is lost from the necrotic core per unit volume of necrotic material is $3s\gamma$ [day^{-1}] where γ [-] is a dimensionless parameter and the three is included for mathematical convenience and consistency with the literature [22]. Therefore, we prescribe the following functions,

$$f_{V_1^{(1)}}\left(R(t);p\right) = sV_1^{(1)}(t) \qquad = s\frac{4\pi}{3}\left(R(t)^3 - R_{\mathrm{n}}(t)^3\right) \tag{5.1}$$

$$f_{V_1^{(2)}}\left(R(t);p\right) = -3s\gamma V_1^{(2)}(t) = -3s\gamma\frac{4\pi}{3}R_{\mathrm{n}}(t)^3 \tag{5.2}$$

To define $R_{\mathrm{n}}(t)$ we consider the oxygen partial pressure within the spheroid. Spatial and temporal differences within spheroids in this study, with respect to cell survival, are reasonably explained by availability of oxygen [7, 56]. Following [56] and our previous study [7], we report oxygen at a radial distance r from the centre of the spheroid and time t, in terms of the oxygen partial pressure $p(r,t)$ [%] for $0 \leq r \leq R(t)$. Oxygen diffuses within the spheroid with diffusivity k [m^2 s^{-1}] and the rate of volume of oxygen gas per unit tumour mass that is consumed by living cells is a constant α [m^3 kg^{-1} s^{-1}]. The external oxygen partial pressure is p_∞ [%]. Since oxygen takes approximately 10 seconds to diffuse across a distance of 100 µm [22], and this timescale is much faster than the timescales of cell proliferation and spheroid growth, we assume that oxygen within the spheroid is at diffusive equilibrium. Therefore, at any instant in time we have $p(r,t) = p(r)$ due to fast diffusion of oxygen. However, as the spheroid is growing with time, diffusion of oxygen occurs on a growing domain and we write $p(r) = p(r(t))$. The governing equation for the oxygen partial pressure within the spheroid, $0 \leq r \leq R(t)$, is,

$$\underbrace{\frac{1}{r^2}\frac{\partial}{\partial r}\left(r^2\frac{\partial}{\partial r}p(r(t))\right)}_{\text{diffusion}} = \underbrace{\frac{\Omega\alpha}{k}\mathrm{H}\left(r - R_{\mathrm{n}}(t)\right)\mathrm{H}\left(R(t) - r\right)}_{\text{consumption in } R_{\mathrm{n}}(t)<r<R(t)}, \tag{6}$$

where $\mathrm{H}(\cdot)$ denotes the Heaviside function and $\Omega = 3.0318 \times 10^7$ [mmHg kg m^{-3}] is a conversion constant from volume of oxygen gas per unit tumour mass to partial pressure. Since we assume that oxygen is only consumed by living cells there is no oxygen consumption in $0 \leq r \leq R_{\mathrm{n}}(t)$. Solving

Eq (6) in each region gives

$$p(r,t) = \begin{cases} p_\infty - \dfrac{\Omega\alpha}{6k}\left[R(t)^2 - r^2\right] + \dfrac{\Omega\alpha}{3k}R_\mathrm{n}(t)^3\left[\dfrac{1}{r} - \dfrac{1}{R(t)}\right], & R_\mathrm{n}(t) \le r \le R(t), \\ p_\infty - \dfrac{\Omega\alpha}{6k}\left[R(t)^2 - R_\mathrm{n}(t)^2 - \dfrac{2R_\mathrm{n}(t)^2}{R(t)}\left(R(t) - R_\mathrm{n}(t)\right)\right], & 0 \le r \le R_\mathrm{n}(t). \end{cases} \tag{7}$$

where we have assumed $p(r,t)$ and $\partial p(r,t)/\partial r$ are continuous at $r = R_\mathrm{n}(t)$, and $p(r,t)$ is bounded at $r = 0$. These assumptions determine constants of integration that arise when solving Eq (6).

We then define $R_\mathrm{n}(t)$ implicitly via

$$p(R_\mathrm{n}(t), t) = p_\mathrm{n}, \tag{8}$$

provided the oxygen partial pressure is sufficiently small, otherwise $R_\mathrm{n}(t) = 0$. Here, p_n [%] corresponds to the oxygen partial pressure threshold below which cells die (Fig 1E,F).

The oxygen partial pressure first reaches p_n at the centre of the spheroid at the end of phase (i) and the start of phase (ii), that we refer to as time T_1. By definition $R_\mathrm{n}(T_1) = 0$. Setting $r = 0$ in the solution of Eq (7) corresponding to the region $R_\mathrm{n}(t) < r < R(t)$ and using Eq (8) we obtain that the radius of the spheroid when the necrotic region first forms, $\mathcal{R}$ [µm], is

$$\mathcal{R}^2 = \frac{6k}{\Omega\alpha}\left(p_\infty - p_\mathrm{n}\right). \tag{9}$$

To obtain an expression for $\mathcal{R}$ in terms of radial measurements $R(t)$ and $R_\mathrm{n}(t)$, and valid for $R(t) > \mathcal{R}$, we evaluate Eq (7) at $r = R_\mathrm{n}(t)$ to obtain

$$\mathcal{R}^2 = R(t)^2 - R_\mathrm{n}(t)^2 - \frac{2R_\mathrm{n}(t)^2}{R(t)}\left[R(t) - R_\mathrm{n}(t)\right]. \tag{10}$$

Substituting the prescribed functions (Eqs (5) and (10)) into general model Eqs (4.1-4.4) gives

$$\frac{\mathrm{d}V_1^{(1)}(t)}{\mathrm{d}t} = s\frac{4\pi}{3}\left(R(t)^3 - R_\mathrm{n}(t)^3\right) - g^{(1)}(R(t);p), \tag{11.1}$$

$$\frac{\mathrm{d}V_1^{(2)}(t)}{\mathrm{d}t} = -3s\gamma\frac{4\pi}{3}R_\mathrm{n}(t)^3 + g^{(1)}(R(t);p), \tag{11.2}$$

$$\frac{\mathrm{d}R(t)}{\mathrm{d}t} = \frac{1}{R(t)^2}\left(\frac{s}{3}\left(R(t)^3 - R_\mathrm{n}(t)^3\right) - s\gamma R_\mathrm{n}(t)^3\right), \tag{11.3}$$

$$g^{(1)}(R(t);p) = s\frac{4\pi}{3}\left(R(t)^3 - R_\mathrm{n}(t)^3\right) - 3s\gamma\frac{4\pi}{3}R_\mathrm{n}(t)^3 - 4\pi\frac{\mathrm{d}R(t)}{\mathrm{d}t}\left(R(t)^2 - R_\mathrm{n}(t)^2\frac{\mathrm{d}R_\mathrm{n}(t)}{\mathrm{d}R(t)}\right), \tag{11.4}$$

$$0 = \begin{cases} R_\mathrm{n}(t) - 0, & R(t) \le \mathcal{R}, \\ -\mathcal{R}^2 + R(t)^2 - R_\mathrm{n}(t)^2 - \dfrac{2R_\mathrm{n}(t)^2}{R(t)}\left(R(t) - R_\mathrm{n}(t)\right), & R(t) > \mathcal{R}. \end{cases} \tag{11.5}$$

In general Eqs (4.1-4.4) are coupled and must be solved simultaneously to obtain $R(t)$ and $R_\mathrm{n}(t)$. Here, for the special case of this monoculture model, Eqs (11.3) and (11.5) can be solved for $R(t)$ and $R_\mathrm{n}(t)$ independently of Eqs (11.1), (11.2), and (11.4). Solving only Eqs (11.3) and (11.5) is the standard formulation of a monoculture compartment-based Greenspan-type model. Therefore, for

consistency with the literature we present the final model as only Eqs (11.3) and (11.5)

$$R(t)^2 \frac{\mathrm{d}R(t)}{\mathrm{d}t} = \frac{s}{3}\left(R(t)^3 - R_\mathrm{n}(t)^3\right) - s\gamma R_\mathrm{n}(t)^3, \tag{12.1}$$

$$0 = \begin{cases} R_\mathrm{n}(t) - 0, & R(t) \leq \mathcal{R}, \\ -\mathcal{R}^2 + R(t)^2 - R_\mathrm{n}(t)^2 - \dfrac{2R_\mathrm{n}(t)}{R(t)}\left(R(t) - R_\mathrm{n}(t)\right), & R(t) > \mathcal{R}, \end{cases} \tag{12.2}$$

where s [day^{-1}] is the rate at which cell volume is produced by mitosis per unit volume of living cells; γ [-] is a dimensionless parameter associated with loss of mass from the necrotic core; $\mathcal{R}$ [µm] is radius of the spheroid when the necrotic region forms associated with the oxygen partial pressure threshold p_n [%]; $R(T)$ [µm] is the initial radius of the spheroid at formation that we treat as a constant parameter; and we set $R_n(T) = 0$ based on experimental observations. This model is characterised by four parameters $\theta = (R(T), s, \gamma, \mathcal{R})$ that we will estimate from our experimental data.

4.3 Co-culture Model 1: Heterogeneous s

Here we extend the monoculture reduced Greenspan model presented in §4.2 by generalising the rate at which cell volume is produced by mitosis per unit volume of living cells, s [day^{-1}], to be two potentially distinct parameters. This results in a model with two populations and two compartments ($I = 2$, $J = 2$). We let population one and two represent melanoma and fibroblast cells, respectively. Accordingly we update the notation and let s_{m} [day^{-1}] and s_{f} [day^{-1}] corresponding to the rates at which cell volume is produced by mitosis per unit volume of living cells for melanoma cells and fibroblasts, respectively (Figure 1I). We assume that the rate at which cell volume is lost from the necrotic core per unit volume of necrotic material is $3s_{\mathrm{m}}\gamma$ [day^{-1}]. All other model assumptions and mechanisms are unchanged. The prescribed functions for Co-culture Model 1 are

$$f_{V_1^{(1)}}\left(R(t);p\right) = s_{\mathrm{m}}V^{(1)}(t)\frac{V_1^{(1)}(t)}{V^{(1)}(t)} = s_{\mathrm{m}}\frac{4\pi}{3}\left(R(t)^3 - R_{\mathrm{n}}(t)^3\right)\frac{V_1^{(1)}(t)}{V_1^{(1)}(t)+V_2^{(1)}(t)}, \tag{13.1}$$

$$f_{V_2^{(1)}}\left(R(t);p\right) = s_{\mathrm{f}}V^{(1)}(t)\frac{V_2^{(1)}(t)}{V^{(1)}(t)} = s_{\mathrm{f}}\frac{4\pi}{3}\left(R(t)^3 - R_{\mathrm{n}}(t)^3\right)\frac{V_2^{(1)}(t)}{V_1^{(1)}(t)+V_2^{(1)}(t)}, \tag{13.2}$$

$$f_{V_1^{(2)}}\left(R(t);p\right) = -3s_{\mathrm{m}}\gamma V^{(2)}(t)\frac{V_1^{(2)}(t)}{V^{(2)}(t)} = -3s_{\mathrm{m}}\gamma\frac{4\pi}{3}R_{\mathrm{n}}(t)^3\frac{V_2^{(2)}(t)}{V_1^{(2)}(t)+V_2^{(2)}(t)}, \tag{13.3}$$

$$f_{V_2^{(2)}}\left(R(t);p\right) = -3s_{\mathrm{m}}\gamma V^{(2)}(t)\frac{V_2^{(2)}(t)}{V^{2}(t)} = -3s_{\mathrm{m}}\gamma\frac{4\pi}{3}R_{\mathrm{n}}(t)^3\frac{V_2^{(2)}(t)}{V_1^{(2)}(t)+V_2^{(2)}(t)}, \tag{13.4}$$

$$0 = \begin{cases} R_{\mathrm{n}}(t) - 0, & R(t) \leq \mathcal{R}, \\ -\mathcal{R}^2 + R(t)^2 - R_{\mathrm{n}}(t)^2 - \dfrac{2R_{\mathrm{n}}(t)^2}{R(t)}\left(R(t) - R_{\mathrm{n}}(t)\right), & R(t) > \mathcal{R}. \end{cases} \tag{13.5}$$

Substituting Eqs (13.1)-(13.5) into Eqs (4.1-4.4) gives

$$\frac{\mathrm{d}V_1^{(1)}(t)}{\mathrm{d}t} = s_{\mathrm{m}}\frac{4\pi}{3}\left(R(t)^3 - R_{\mathrm{n}}(t)^3\right)\frac{V_1^{(1)}(t)}{V_1^{(1)}(t)+V_2^{(1)}(t)} - g^{(1)}(R(t);p)\frac{V_1^{(1)}(t)}{V_1^{(1)}(t)+V_2^{(1)}(t)}, \tag{14.1}$$

$$\frac{\mathrm{d}V_2^{(1)}(t)}{\mathrm{d}t} = s_{\mathrm{f}}\frac{4\pi}{3}\left(R(t)^3 - R_{\mathrm{n}}(t)^3\right)\frac{V_2^{(1)}(t)}{V_1^{(1)}(t)+V_2^{(1)}(t)} - g^{(1)}(R(t);p)\frac{V_2^{(1)}(t)}{V_1^{(1)}(t)+V_2^{(1)}(t)}, \tag{14.2}$$

$$\frac{\mathrm{d}V_1^{(2)}(t)}{\mathrm{d}t} = -3s_{\mathrm{m}}\gamma\frac{4\pi}{3}R_{\mathrm{n}}(t)^3\frac{V_2^{(2)}(t)}{V_1^{(2)}(t)+V_2^{(2)}(t)} + g^{(1)}(R(t);p)\frac{V_1^{(1)}(t)}{V_1^{(1)}(t)+V_2^{(1)}(t)}, \tag{14.3}$$

$$\frac{\mathrm{d}V_2^{(2)}(t)}{\mathrm{d}t} = -3s_{\mathrm{m}}\gamma\frac{4\pi}{3}R_{\mathrm{n}}(t)^3\frac{V_2^{(2)}(t)}{V_1^{(2)}(t)+V_2^{(2)}(t)} + g^{(1)}(R(t);p)\frac{V_2^{(1)}(t)}{V_1^{(1)}(t)+V_2^{(1)}(t)}, \tag{14.4}$$

$$\frac{\mathrm{d}R(t)}{\mathrm{d}t} = \frac{1}{R(t)^2}\left[\left(\frac{s_{\mathrm{m}}}{3}\frac{V_1^{(1)}(t)}{V_1^{(1)}(t)+V_2^{(1)}(t)} + \frac{s_2}{3}\frac{V_2^{(1)}(t)}{V_1^{(1)}(t)+V_2^{(1)}(t)}\right)\left(R(t)^3 - R_{\mathrm{n}}(t)^3\right) - s_1\gamma R_{\mathrm{n}}(t)^3\right], \tag{14.5}$$

$$\begin{aligned} g^{(1)}(R(t);p) = {} & \frac{4\pi}{3}\left[\left(\frac{s_{\mathrm{m}}}{3}\frac{V_1^{(1)}(t)}{V_1^{(1)}(t)+V_2^{(1)}(t)} + \frac{s_2}{3}\frac{V_2^{(1)}(t)}{V_1^{(1)}(t)+V_2^{(1)}(t)}\right)\left(R(t)^3 - R_{\mathrm{n}}(t)^3\right)\right] \\ & - 4\pi\frac{\mathrm{d}R(t)}{\mathrm{d}t}\left(R(t)^2 - R_{\mathrm{n}}(t)^2\frac{\mathrm{d}R_{\mathrm{n}}(t)}{\mathrm{d}R(t)}\right). \end{aligned} \tag{14.6}$$

For Eq (14.6) we obtain $\mathrm{d}R_{\mathrm{n}}(t)/\mathrm{d}R(t)$ by differentiating Eq (13.5) with respect to $R(t)$ and rearranging

$$\frac{\mathrm{d}R_{\mathrm{n}}(t)}{\mathrm{d}R(t)} = \begin{cases} 0, & \text{for } R(t) \leq \mathcal{R}, \\ \dfrac{2R(t) + \dfrac{2R_{\mathrm{n}}(t)^2}{R(t)^2}\left(R(t) - R_{\mathrm{n}}(t)\right) - \dfrac{2R_{\mathrm{n}}(t)^2}{R(t)}}{2R_{\mathrm{n}}(t) + \dfrac{4R_{\mathrm{n}}(t)}{R(t)}\left(R(t) - R_{\mathrm{n}}(t)\right) - \dfrac{2R_{\mathrm{n}}(t)^2}{R(t)}}, & \text{for } R(t) > \mathcal{R}. \end{cases} \tag{15}$$

We solve the system of Eqs (14.1)-(14.6) with Eqs (13.5) and (15) numerically. To specify initial conditions we introduce $V_{\mathrm{m}}(T) = V_1(T)$ as the volume of melanoma cells at spheroid formation, $t = T$, and treat this as a parameter. The volume of fibroblast cells at $t = T$ is then $V_2(T) = V_{\mathrm{f}}(T) = 4\pi R(T)^3/3 - V_{\mathrm{m}}(T)$. This model is characterised by six parameters $\theta = (R(T), V_{\mathrm{m}}(T), s_{\mathrm{m}}, s_{\mathrm{f}}, \gamma, \mathcal{R})$ that we will estimate from our experimental data.

4.4 Co-culture Model 2: Heterogeneous γ

Here we extend the monoculture reduced Greenspan model presented in §4.2 by generalising the dimensionless parameter γ associated with rate at which mass is lost from the necrotic core to be two potentially distinct parameters. This results in a model with two populations and two compartments ($I = 2$, $J = 2$). We let population one and two represent melanoma and fibroblast cells, respectively. We assume that the rate at which cell volume is lost from the necrotic core per unit volume of necrotic material is $3s\gamma_m$ [day^{-1}] for melanoma cells and is $3s\gamma_m$ [day^{-1}] for fibroblasts. All other model assumptions and mechanisms are unchanged. The prescribed functions for Co-culture Model 2 are

$$f_{V_1^{(1)}}\left(R(t);p\right) = sV^{(1)}(t)\frac{V_1^{(1)}(t)}{V^{(1)}(t)} = s\frac{4\pi}{3}\left(R(t)^3 - R_{\mathrm{n}}(t)^3\right)\frac{V_1^{(1)}(t)}{V_1^{(1)}(t)+V_2^{(1)}(t)}, \tag{16.1}$$

$$f_{V_2^{(1)}}\left(R(t);p\right) = sV^{(1)}(t)\frac{V_2^{(1)}(t)}{V^{(1)}(t)} = s\frac{4\pi}{3}\left(R(t)^3 - R_{\mathrm{n}}(t)^3\right)\frac{V_2^{(1)}(t)}{V_1^{(1)}(t)+V_2^{(1)}(t)}, \tag{16.2}$$

$$f_{V_1^{(2)}}\left(R(t);p\right) = -3s\gamma_{\mathrm{m}}V^{(2)}(t)\frac{V_1^{(2)}(t)}{V^{(2)}(t)} = -3s\gamma_{\mathrm{m}}\frac{4\pi}{3}R_{\mathrm{n}}(t)^3\frac{V_2^{(2)}(t)}{V_1^{(2)}(t)+V_2^{(2)}(t)}, \tag{16.3}$$

$$f_{V_2^{(2)}}\left(R(t);p\right) = -3s\gamma_{\mathrm{f}}V^{(2)}(t)\frac{V_2^{(2)}(t)}{V^{2}(t)} = -3s\gamma_{\mathrm{f}}\frac{4\pi}{3}R_{\mathrm{n}}(t)^3\frac{V_2^{(2)}(t)}{V_1^{(2)}(t)+V_2^{(2)}(t)}, \tag{16.4}$$

$$0 = \begin{cases} R_{\mathrm{n}}(t) - 0, & R(t) \le \mathcal{R}, \\ -\mathcal{R}^2 + R(t)^2 - R_{\mathrm{n}}(t)^2 - \dfrac{2R_{\mathrm{n}}(t)^2}{R(t)}\left(R(t) - R_{\mathrm{n}}(t)\right), & R(t) > \mathcal{R}. \end{cases} \tag{16.5}$$

Substituting Eqs (16.1-16.5) into Eqs (4.1-4.4) gives

$$\frac{\mathrm{d}V_1^{(1)}(t)}{\mathrm{d}t} = s_{\mathrm{m}}\frac{4\pi}{3}\left(R(t)^3 - R_{\mathrm{n}}(t)^3\right)\frac{V_1^{(1)}(t)}{V_1^{(1)}(t)+V_2^{(1)}(t)} - g^{(1)}(R(t);p)\frac{V_1^{(1)}(t)}{V_1^{(1)}(t)+V_2^{(1)}(t)}, \tag{17.1}$$

$$\frac{\mathrm{d}V_2^{(1)}(t)}{\mathrm{d}t} = s_{\mathrm{f}}\frac{4\pi}{3}\left(R(t)^3 - R_{\mathrm{n}}(t)^3\right)\frac{V_2^{(1)}(t)}{V_1^{(1)}(t)+V_2^{(1)}(t)} - g^{(1)}(R(t);p)\frac{V_2^{(1)}(t)}{V_1^{(1)}(t)+V_2^{(1)}(t)}, \tag{17.2}$$

$$\frac{\mathrm{d}V_1^{(2)}(t)}{\mathrm{d}t} = -3s_{\mathrm{m}}\gamma\frac{4\pi}{3}R_{\mathrm{n}}(t)^3\frac{V_2^{(2)}(t)}{V_1^{(2)}(t)+V_2^{(2)}(t)} + g^{(1)}(R(t);p)\frac{V_1^{(1)}(t)}{V_1^{(1)}(t)+V_2^{(1)}(t)}, \tag{17.3}$$

$$\frac{\mathrm{d}V_2^{(2)}(t)}{\mathrm{d}t} = -3s_{\mathrm{m}}\gamma\frac{4\pi}{3}R_{\mathrm{n}}(t)^3\frac{V_2^{(2)}(t)}{V_1^{(2)}(t)+V_2^{(2)}(t)} + g^{(1)}(R(t);p)\frac{V_2^{(1)}(t)}{V_1^{(1)}(t)+V_2^{(1)}(t)}, \tag{17.4}$$

$$\frac{\mathrm{d}R(t)}{\mathrm{d}t} = \frac{1}{R(t)^2}\left[\left(\frac{s_{\mathrm{m}}}{3}\frac{V_1^{(1)}(t)}{V_1^{(1)}(t)+V_2^{(1)}(t)} + \frac{s_2}{3}\frac{V_2^{(1)}(t)}{V_1^{(1)}(t)+V_2^{(1)}(t)}\right)\left(R(t)^3 - R_{\mathrm{n}}(t)^3\right) - s_1\gamma R_{\mathrm{n}}(t)^3\right], \tag{17.5}$$

$$\begin{aligned} g^{(1)}(R(t);p) = {} & \frac{4\pi}{3}\left[\left(\frac{s_{\mathrm{m}}}{3}\frac{V_1^{(1)}(t)}{V_1^{(1)}(t)+V_2^{(1)}(t)} + \frac{s_2}{3}\frac{V_2^{(1)}(t)}{V_1^{(1)}(t)+V_2^{(1)}(t)}\right)\left(R(t)^3 - R_{\mathrm{n}}(t)^3\right)\right] \\ & - 4\pi\frac{\mathrm{d}R(t)}{\mathrm{d}t}\left(R(t)^2 - R_{\mathrm{n}}(t)^2\frac{\mathrm{d}R_{\mathrm{n}}(t)}{\mathrm{d}R(t)}\right). \end{aligned} \tag{17.6}$$

For Eq (17.6) $\mathrm{d}R_{\mathrm{n}}(t)/\mathrm{d}R(t)$ is given by Eq (15). We solve the system of Eqs (17.1)-(17.6) with Eqs (16.1 and (15) numerically. This model is characterised by six parameters $\theta = (R(T), V_{\mathrm{m}}(T), s, \gamma_{\mathrm{m}}, \gamma_{\mathrm{f}}, \mathcal{R})$ that we will estimate from our experimental data.

4.5 Co-culture Model 3: Heterogeneous $\mathcal{R}$

Here we extend the monoculture reduced Greenspan model (§4.2) by generalising the single oxygen partial pressure threshold p_{n} [%] to two potentially distinct parameters p_{m} [%] and p_{f} [%]. The new parameters p_{m} and p_{f} correspond to the oxygen partial pressure below which melanoma (population 1) and fibroblast (population 2) cells die, respectively (Figure 1K,L). We assume $p_{\mathrm{f}} \geq p_{\mathrm{m}}$ to reproduce experimental observations with regards to the position of fibroblasts within the spheroid. Generalising p_{n} corresponds to generalising the parameter $\mathcal{R}$ (Eq 9) to two potentially distinct parameters $\mathcal{R}_{\mathrm{m}}$ [µm] and $\mathcal{R}_{\mathrm{f}}$ [µm]. The new parameters $\mathcal{R}_{\mathrm{m}}$ and $\mathcal{R}_{\mathrm{f}}$ depend on p_{m} and p_{f}, respectively.

The resulting model describes two populations with three compartments ($I = 2$, $J = 3$). In phase (i) all cells proliferate and the spheroid grows exponentially. In phase (ii), the in $R_{\mathrm{f}}(t) \leq r \leq R(t)$ melanoma cells and fibroblasts proliferate and in $0 \leq r \leq R_{\mathrm{f}}(t)$ melanoma cells proliferate and fibroblasts are necrotic. In phase (iii), in compartment one, $R_{\mathrm{f}}(t) \leq r \leq R(t)$, melanoma cells and fibroblasts proliferate; in compartment two, $R_{\mathrm{m}}(t) \leq r \leq R_{\mathrm{f}}(t)$, melanoma cells proliferate while in fibroblasts are necrotic; and in compartment three, $0 \leq r \leq R_{\mathrm{m}}(t)$, melanoma and fibroblast cells are necrotic. We define $R_{\mathrm{m}}(t)$ and $R_{\mathrm{f}}(t)$ through geometric constraints obtained by considering oxygen diffusion, consumption, and the thresholds p_{m} and p_{f}, respectively. All other model assumptions and mechanisms are unchanged. The prescribed functions for Co-culture Model 3 are

$$f_{V_1^{(1)}}\left(R(t);p\right) = sV^{(1)}(t)\frac{V_1^{(1)}(t)}{V^{(1)}(t)} = s\frac{4\pi}{3}\left(R(t)^3 - R_{\mathrm{f}}(t)^3\right)\frac{V_1^{(1)}(t)}{V_1^{(1)}(t)+V_2^{(1)}(t)}, \tag{18.1}$$

$$f_{V_2^{(1)}}\left(R(t);p\right) = sV^{(1)}(t)\frac{V_2^{(1)}(t)}{V^{(1)}(t)} = s\frac{4\pi}{3}\left(R(t)^3 - R_{\mathrm{f}}(t)^3\right)\frac{V_2^{(1)}(t)}{V_1^{(1)}(t)+V_2^{(1)}(t)}, \tag{18.2}$$

$$f_{V_1^{(2)}}\left(R(t);p\right) = sV^{(2)}(t)\frac{V_1^{(2)}(t)}{V^{(2)}(t)} = s\frac{4\pi}{3}\left(R_{\mathrm{f}}(t)^3 - R_{\mathrm{m}}(t)^3\right)\frac{V_1^{(2)}(t)}{V_1^{(2)}(t)+V_2^{(2)}(t)}, \tag{18.3}$$

$$f_{V_2^{(2)}}\left(R(t);p\right) = -3s\gamma V^{(2)}(t)\frac{V_2^{(2)}(t)}{V^{2}(t)} = -3s\gamma\frac{4\pi}{3}\left(R_{\mathrm{f}}(t)^3 - R_{\mathrm{m}}(t)^3\right)\frac{V_2^{(2)}(t)}{V_1^{(2)}(t)+V_2^{(2)}(t)}, \tag{18.4}$$

$$f_{V_1^{(3)}}\left(R(t);p\right) = -3s\gamma V^{(3)}(t)\frac{V_1^{(3)}(t)}{V^{(3)}(t)} = -3s\gamma\frac{4\pi}{3}R_{\mathrm{m}}(t)^3\frac{V_1^{(3)}(t)}{V_1^{(3)}(t)+V_2^{(3)}(t)}, \tag{18.5}$$

$$f_{V_2^{(3)}}\left(R(t);p\right) = -3s\gamma V^{(3)}(t)\frac{V_2^{(3)}(t)}{V^{3}(t)} = -3s\gamma\frac{4\pi}{3}R_{\mathrm{m}}(t)^3\frac{V_2^{(3)}(t)}{V_1^{(3)}(t)+V_2^{(3)}(t)}. \tag{18.6}$$

To define $R_{\mathrm{m}}(t)$ and $R_{\mathrm{f}}(t)$ we consider the oxygen partial pressure within the spheroid. In agreement with the two compartment model, spatial and temporal differences within spheroids in this study, with respect to cell survival, are thought to arise due to availability of oxygen. Considering the proportion of each population in each region of the spheroid and recalling that only living cells consume oxygen, the governing equation for the oxygen partial pressure within the spheroid is

$$\underbrace{\frac{1}{r^2}\frac{\partial}{\partial r}\left(r^2\frac{\partial}{\partial r}p(r(t))\right)}_{\text{diffusion}} = \begin{cases} \dfrac{\Omega\alpha}{k}, & R_{\mathrm{f}}(t) \leq r \leq R(t), \\ \dfrac{\Omega\alpha}{k}\dfrac{V_1^{(2)}(t)}{V_1^{(2)}(t)+V_2^{(2)}(t)}, & R_{\mathrm{m}}(t) \leq r \leq R_{\mathrm{f}}(t), \\ 0, & 0 \leq r \leq R_{\mathrm{m}}(t). \end{cases} \tag{19}$$

Oxygen within the spheroid is assumed to be at diffusive equilibrium and we assume that oxygen diffusion is fast relative to the migration of cells across the compartment boundaries. Under these assumptions we treat $\phi = V_1^{(2)}(t)/\left(V_1^{(2)}(t) + V_2^{(2)}(t)\right)$ as constant at each time point and solve Eq (19) analytically

$$p(r,t) = \begin{cases} p_\infty + \dfrac{\Omega\alpha}{6k}\dfrac{1}{rR(t)}\Big[-\left(rR(t)^2 + R(t)r^2 + \left(2R_{\mathrm{f}}(t)^3 - 2R_{\mathrm{m}}(t)^3\right)\phi \right. \\ \qquad \left. -2R_{\mathrm{f}}(t)^3\right)\left(-r + R(t)\right)\Big], & R_{\mathrm{f}}(t) \le r \le R(t), \\ p_\infty + \dfrac{\Omega\alpha}{6k}\dfrac{1}{rR(t)}\Big[\phi r^3 R(t) + \Big(-R(t)^3 - 3\,R_{\mathrm{f}}(t)^2\,(\phi-1)\,R(t) \\ \qquad + \left(2\,R_{\mathrm{f}}(t)^3 - 2\,R_{\mathrm{m}}(t)^3\right)\phi - 2\,R_{\mathrm{f}}(t)^3\Big)r + 2\,R_{\mathrm{m}}(t)^3\phi R(t)\Big], & R_{\mathrm{m}}(t) \le r \le R_{\mathrm{f}}(t), \\ p_\infty + \dfrac{\Omega\alpha}{6k}\dfrac{1}{R(t)}\Big[-R(t)^3 + \left(\left(-3\,R_{\mathrm{f}}(t)^2 + 3\,R_{\mathrm{m}}(t)^2\right)\phi + 3\,R_{\mathrm{f}}(t)^2\right)R(t) \\ \qquad + \left(2\,R_{\mathrm{f}}(t)^3 - 2\,R_{\mathrm{m}}(t)^3\right)\phi - 2\,R_{\mathrm{f}}(t)^3\Big], & 0 \le r \le R_{\mathrm{m}}(t). \end{cases} \tag{20}$$

where we have assumed $p(r,t)$ and $\partial p(r,t)/\partial r$ are continuous at $r = R_{\mathrm{m}}(t)$ and $r = R_{\mathrm{f}}(t)$, and $p(r,t)$ is bounded at $r = 0$ to determine the constants of integration that arise when solving Eq (20).

The two oxygen partial pressure thresholds, p_{f} and p_{m}, define $R_{\mathrm{f}}(t)$ and $R_{\mathrm{m}}(t)$ via (Fig 1K,L)

$$p(R_{\mathrm{f}}(t), t) = p_{\mathrm{f}}, \tag{21.1}$$

$$p(R_{\mathrm{m}}(t), t) = p_{\mathrm{m}}. \tag{21.2}$$

The oxygen partial pressure first reaches the oxygen partial pressure threshold p_{f} at $t = T_1$, corresponding to the end of phase (i) and the start of phase (ii). By definition $R_{\mathrm{f}}(T_1) = 0$ and $R_{\mathrm{m}}(T_1) = 0$. Setting $r = 0$ in the region $R_{\mathrm{f}}(t) < r < R(t)$ of Eq (20) and using Eq (21.1) we obtain that the radius of the spheroid when fibroblasts first undergo necrosis, $\mathcal{R}_{\mathrm{f}}$ [µm], is

$$\mathcal{R}_{\mathrm{f}}^2 = \frac{6k}{\Omega\alpha}\left(p_\infty - p_{\mathrm{f}}\right). \tag{22}$$

The oxygen partial pressure first reaches p_{m} at the centre of the spheroid at $t = T_2$, corresponding to the end of phase (ii) and start of phase (iii). By definition $R_{\mathrm{f}}(T_3) > 0$ and $R_{\mathrm{m}}(T_2) = 0$. Setting $r = 0$ in the region $R_{\mathrm{m}}(t) < r < R_{\mathrm{f}}(t)$ of Eq (20) and using Eq (21.2) we obtain,

$$\mathcal{R}_{\mathrm{m}}^2 = -\frac{1}{R(t)}\left[-R(t)^3 - 3R_{\mathrm{f}}(t)^2\,(\phi-1)\,R(t) + 2R_{\mathrm{f}}(t)^3\,(\phi-1)\right], \tag{23}$$

where

$$\mathcal{R}_{\mathrm{m}}^2 = \frac{6k}{\Omega\alpha}\left(p_\infty - p_{\mathrm{m}}\right). \tag{24}$$

Setting $\phi = 1$ in Eq (23) gives $\mathcal{R}_{\mathrm{m}} = R(t)$. Hence, $\mathcal{R}_{\mathrm{m}}$ is the radius of a monoculture melanoma spheroid when the necrotic region first forms. Note Eq (23) is only valid at $t = T_2$.

To obtain expressions for $\mathcal{R}_{\mathrm{f}}$ and $\mathcal{R}_{\mathrm{m}}$ throughout time and in terms of radial measurements, $R(t)$, $R_{\mathrm{f}}(t)$, and $R_{\mathrm{m}}(t)$, we evaluate Eq (20) at $r = R_{\mathrm{f}}(t)$ and $r = R_{\mathrm{m}}(t)$, respectively, and use Eqs (21.1) and (21.2) to obtain

$$\mathcal{R}_{\mathrm{f}}^2 = -\frac{1}{R_{\mathrm{f}}(t)R(t)}\Bigg[-\Big(R_{\mathrm{f}}(t)R(t)^2 + R(t)R_{\mathrm{f}}(t)^2 + \left(2R_{\mathrm{f}}(t)^3 - 2R_{\mathrm{m}}(t)^3\right)\phi - 2R_{\mathrm{f}}(t)^3\Big)\Big(-R_{\mathrm{f}}(t) + R(t)\Big)\Bigg], \qquad t > T_1, \tag{25}$$

$$\mathcal{R}_{\mathrm{m}}^2 = -\frac{1}{R_{\mathrm{m}}(t)R(t)}\Bigg[3\phi R_{\mathrm{m}}(t)^3 R(t) + \Big(-R(t)^3 - 3\,R_{\mathrm{f}}(t)^2\,(\phi-1)\,R(t) + \left(2\,R_{\mathrm{f}}(t)^3 - 2\,R_{\mathrm{m}}(t)^3\right)\phi - 2\,R_{\mathrm{f}}(t)^3\Big)R_{\mathrm{m}}(t)\Bigg], \quad t > T_2. \tag{26}$$

Assuming $R(t)$ and $\mathcal{R}_{\mathrm{f}}$ and $\mathcal{R}_{\mathrm{f}}$ are known, we determine the geometric constraints that define $R_{\mathrm{f}}(t)$ and $R_{\mathrm{m}}(t)$, respectively, through

$$0 = \begin{cases} R_{\mathrm{f}}(t) - 0, & 0 \le t \le T_1, \\ -\mathcal{R}_{\mathrm{f}}^2 - \dfrac{1}{R_{\mathrm{f}}(t)R(t)}\Bigg[-\Big(R_{\mathrm{f}}(t)R(t)^2 + R(t)R_{\mathrm{f}}(t)^2 + 2R_{\mathrm{f}}(t)^3\,(\phi-1)\Big)\Big(-R_{\mathrm{f}}(t) + R(t)\Big)\Bigg], & T_1 < t \le T_2, \\ -\mathcal{R}_{\mathrm{f}}^2 - \dfrac{1}{R_{\mathrm{f}}(t)R(t)}\Bigg[-\Big(R_{\mathrm{f}}(t)R(t)^2 + R(t)R_{\mathrm{f}}(t)^2 + \left(2R_{\mathrm{f}}(t)^3 - 2R_{\mathrm{m}}(t)^3\right)\phi - 2R_{\mathrm{f}}(t)^3\Big)\Big(-R_{\mathrm{f}}(t) + R(t)\Big)\Bigg], & t > T_2, \end{cases} \tag{27}$$

$$0 = \begin{cases} R_{\mathrm{m}}(t) - 0, & 0 \le t \le T_2, \\ -\mathcal{R}_{\mathrm{m}}^2 - \dfrac{1}{R_{\mathrm{m}}(t)R(t)}\Bigg[3\phi R_{\mathrm{m}}(t)^3 R(t) + \Big(-R(t)^3 - 3\,R_{\mathrm{f}}(t)^2\,(\phi-1)\,R(t) + \left(2\,R_{\mathrm{f}}(t)^3 - 2\,R_{\mathrm{m}}(t)^3\right)\phi - 2\,R_{\mathrm{f}}(t)^3\Big)R_{\mathrm{m}}(t)\Bigg], & t > T_2, \end{cases} \tag{28}$$

Given these expressions we determine $\mathrm{d}R_{\mathrm{f}}(t)/\mathrm{d}R(t)$ and $\mathrm{d}R_{\mathrm{m}}(t)/\mathrm{d}R(t)$ by considering phase (ii) and phase (iii) separately. For phase (ii), we implicitly differentiate Eq (27) with respect to $R(t)$ to obtain

$$\frac{\mathrm{d}R_{\mathrm{f}}(t)}{\mathrm{d}R(t)} = \frac{(\phi-1)\,R_{\mathrm{f}}(t)^3 + R(t)^3}{R(t)R_{\mathrm{f}}(t)\left[3R_{\mathrm{f}}(t)\phi - 2R(t)\phi - 3R_{\mathrm{f}}(t) + 3R(t)\right]}, \tag{29}$$

where as before we set $\phi = V_1^{(2)}(t)/\left(V_1^{(2)}(t) + V_2^{(2)}(t)\right)$. For phase (iii) we implicitly differentiate Eqs (27) and (28) with respect to $R(t)$, and solve the resulting two coupled differential equations for $\mathrm{d}R_{\mathrm{f}}(t)/\mathrm{d}R(t)$ and $\mathrm{d}R_{\mathrm{m}}(t)/\mathrm{d}R(t)$,

$$\frac{\mathrm{d}R_{\mathrm{f}}(t)}{\mathrm{d}R(t)} = \frac{-R_{\mathrm{f}}(t)\left((\phi-1)\,R_1(t)^3 - R_{\mathrm{m}}(t)^3\phi + R(t)^3\right)}{2R(t)\left[\frac{3}{2}\,(1-\phi)\,R_{\mathrm{f}}(t)^3 + \left(\frac{R_{\mathrm{m}}(t)\phi}{2} + R(t)\left(\phi - \frac{3}{2}\right)\right)R_{\mathrm{f}}(t)^2 - \frac{R_{\mathrm{m}}(t)\phi(R(t)-R_{\mathrm{m}}(t))R_{\mathrm{f}}(t)}{2} - \frac{\phi R_{\mathrm{m}}(t)^2(R(t)-R_{\mathrm{m}}(t))}{2}\right]}, \tag{30.1}$$

$$\frac{\mathrm{d}R_{\mathrm{m}}(t)}{\mathrm{d}R(t)} = \frac{-\left(R_{\mathrm{f}}(t)^2 + R_{\mathrm{m}}(t)R_{\mathrm{f}}(t) + R_{\mathrm{m}}(t)^2\right)\left((\phi-1)\,R_{\mathrm{f}}(t)^3 - R_{\mathrm{m}}(t)^3\phi + R(t)^3\right)}{6R(t)\left[\frac{3}{2}\,(1-\phi)\,R_{\mathrm{f}}(t)^3 + \left(\frac{R_{\mathrm{m}}(t)\phi}{2} + R(t)\left(\phi - \frac{3}{2}\right)\right)R_{\mathrm{f}}(t)^2 - \frac{R_{\mathrm{m}}(t)\phi(R(t)-R_{\mathrm{m}}(t))R_{\mathrm{f}}(t)}{2} - \frac{\phi R_{\mathrm{m}}(t)^2(R(t)-R_{\mathrm{m}}(t))}{2}\right]R_{\mathrm{m}}(t)}. \tag{30.2}$$

Substituting Eqs (18.1)-(18.6), (27), (28), 29, and (30) into Eqs (4.1-4.4) gives the final system that we solve numerically. This model is characterised by six parameters $\theta = (R(T), V_{\mathrm{m}}(T), s, \gamma, \mathcal{R}_{\mathrm{m}}, \mathcal{R}_{\mathrm{f}})$ that we will estimate from our experimental data.

4.6 Co-culture Model 4: Heterogeneous $\mathcal{R}$ and additional cell migration

To capture experimental results where fibroblasts are positioned throughout the spheroid at early times but are only observed in the central region of the spheroid at later times we extend Co-culture Model 3 (§4.5). We now include an additional cell migration mechanism that we denote $h(R(t);p)$. There are many biological reasons why this migration could occur and this model does not rule in or out any possibility. We assume $h(R(t);p)$ is known either from a modelling assumption or by considering additional biological mechanisms. Here, we assume that population 1 (melanoma) cells in region 2 migrate to region 1 while the same volume of population 2 (fibroblast) cells in region 1 migrate to region 2. Then we prescribe $h(R(t);p)$ in Eq (31.7) by taking a simple approach and assuming that $h(R(t);p)$ depends on the volume of population 2 (fibroblasts) cells in region 2, the volume of population 1 (melanoma) cells in region 1, and a new parameter ω. Therefore, $h(R(t);p) = 0$ if $V_1^{(1)}(t) = 0$ or $V_2^{(2)}(t) = 0$. Alternative choices could be considered. The prescribed functions for Co-culture Model 4 are

$$f_{V_1}^{(1)}(R(t);p) = \frac{4\pi}{3} s \left(R(t)^3 - R_{\mathrm{f}}(t)^3\right) \frac{V_1^{(1)}(t)}{V_1^{(1)}(t) + V_2^{(1)}(t)} + \underbrace{h(R(t);p)}_{\text{additional migration}}, \tag{31.1}$$

$$f_{V_2}^{(1)}(R(t);p) = \frac{4\pi}{3} s \left(R(t)^3 - R_{\mathrm{f}}(t)^3\right) \frac{V_2^{(1)}(t)}{V_1^{(1)}(t) + V_2^{(1)}(t)} - \underbrace{h(R(t);p)}_{\text{additional migration}}, \tag{31.2}$$

$$f_{V_1}^{(2)}(R(t);p) = \frac{4\pi}{3} s \left(R_{\mathrm{f}}(t)^3 - R_{\mathrm{m}}(t)^3\right) \frac{V_1^{(2)}(t)}{V_1^{(2)}(t) + V_2^{(2)}(t)} - \underbrace{h(R(t);p)}_{\text{additional migration}}, \tag{31.3}$$

$$f_{V_2}^{(2)}(R(t);p) = -\frac{4\pi}{3} 3 s\gamma \left(R_{\mathrm{f}}(t)^3 - R_{\mathrm{m}}(t)^3\right) \frac{V_2^{(2)}(t)}{V_1^{(2)}(t) + V_2^{(2)}(t)} + \underbrace{h(R(t);p)}_{\text{additional migration}}, \tag{31.4}$$

$$f_{V_1}^{(3)}(R(t);p) = -\frac{4\pi}{3} 3 s\gamma R_{\mathrm{m}}(t)^3 \frac{V_1^{(3)}(t)}{V_1^{(3)}(t) + V_2^{(3)}(t)}, \tag{31.5}$$

$$f_{V_2}^{(3)}(R(t);p) = -\frac{4\pi}{3} 3 s\gamma R_{\mathrm{m}}(t)^3 \frac{V_2^{(3)}(t)}{V_1^{(3)}(t) + V_2^{(3)}(t)}, \tag{31.6}$$

$$h(R(t);p) = \omega \underbrace{\frac{4\pi}{3} \left(R(t)^3 - R_{\mathrm{f}}(t)^3\right) \frac{V_2^{(1)}(t)}{V_1^{(1)}(t) + V_2^{(1)}(t)}}_{\text{volume of fibroblasts in } R_{\mathrm{f}}(t)<r<R(t)} \underbrace{\frac{4\pi}{3} \left(R_{\mathrm{f}}(t)^3 - R_{\mathrm{m}}(t)^3\right) \frac{V_1^{(2)}(t)}{V_1^{(2)}(t) + V_2^{(2)}(t)}}_{\text{volume of melanoma cells in } R_{\mathrm{m}}(t)<r<R_{\mathrm{f}}(t)}. \tag{31.7}$$

This model is characterised by seven parameters $\theta = (R(T), V_{\mathrm{m}}(T), s, \gamma, \mathcal{R}_{\mathrm{m}}, \mathcal{R}_{\mathrm{f}}, \omega)$ that we will estimate from our experimental data.

5 Parameter identifiability analysis and estimation

For each deterministic mathematical model shown in §3-§4 we assess if the model parameters are practically identifiable and perform parameter estimation using profile likelihood analysis [6, 15, 19, 20]. For this purpose we assume that experimental measurements are noisy observations of the deterministic mathematical model. Therefore, we couple each deterministic mathematical model with a probabilistic observation model, also referred to as an error model. The probabilistic observation model accounts for experimental variability and measurement error. We assume that observation errors are independent, identically distributed, additive and normally distributed with zero mean and constant variance σ^2. We estimate σ alongside other model parameters. For the biphasic model (Eq (1)) and linear model (Eq (2)) experimental measurements comprise of estimates of the radius of each spheroid, $R(t)$. For the compartment-based models in §4 experimental measurements comprise of estimates of the radius of each spheroid, $R(t)$, and the necrotic core of each spheroid, $R_{\mathrm{n}}(t)$.

For this approach we use the log-likelihood function $\ell(\theta|y^{\mathrm{o}}_{1:J}) = \sum_{j=1}^{J} \log[\phi(y^{\mathrm{o}}_j; y_j(\theta), \sigma^2(\theta))]$, where $\phi(x; \mu, \sigma^2)$ denotes a Gaussian probability density function with mean μ and constant variance σ^2; θ denotes model parameters; and y^{o}_j denotes the jth experimental observation. For a best-fit to the data we compute the maximum likelihood estimate (MLE), $\hat{\theta} = \sup_\theta \ell(\theta|y^{\mathrm{o}}_{1:J})$, subject to bound constraints. Results are reported in terms of the normalised log-likelihood function, $\hat{\ell}(\theta|y^{\mathrm{o}}_{1:J}) = \ell(\theta|y^{\mathrm{o}}_{1:J}) - \sup_\theta \ell(\theta|y^{\mathrm{o}})$. Note $\hat{\ell}(\hat{\theta}|y^{\mathrm{o}}_{1:J}) = 0$. To compute profile likelihoods we assume that the full parameter θ can be partitioned into $\theta = (\psi, \lambda)$, where ψ is a scalar interest parameter and λ is a vector nuisance parameter. The profile likelihood for ψ is $\hat{\ell}_p(\psi|y^{\mathrm{o}}) = \sup_\lambda \ell(\psi, \lambda|y^{\mathrm{o}}_{1:J})$. Bounds are chosen to ensure that approximate 95% confidence intervals, defined using a profile likelihood threshold value of -1.92 [58], are captured. Mathematical models are solved numerically using the open-source `DifferentialEquations` package in Julia (Supplementary S3). Numerical optimisations are performed using the Nelder–Mead routine in the open-source `NLopt` optimisation package in Julia [59], for further detail see [15].

6 Results and discussion

Here we analyse spheroid formation, geometry, and growth of overall size and structure in co-culture experiments. Throughout we consider four conditions (M100:F0, M75:F25, M50:F50, M25:F75, where Mx:Fy is the initial proportion, measured as a percentage, of melanoma cells x [%] and fibroblasts $y = 100 - x$ [%] at the time of seeding). We seek to provide mechanistic insight by analysing experimental measurements of $R(t)$ and $R_{\mathrm{n}}(t)$ within objective mathematical and statistical modelling framework presented in §3-§5.

6.1 Spheroid formation and geometry

Spheroid experiments are routinely performed to characterise cancer growth. Fibroblasts are commonly included in cancer cell line experiments to enhance spheroid formation and structure. For example, compare the size and densities of 1205Lu monoculture (M100:F0) spheroids and monoculture fibroblast (M0:F100) spheroids (Fig 4A). In both conditions cells initially placed in the well migrate and adhere. The M0:F100 spheroid forms a compact, dense, and approximately spherical structure by approximately 48 hours. In contrast, the M100:F0 spheroid does not (Fig 4B). Experimental images for intermediate conditions, namely M75:F25, M50:F50, and M25:F75, show that fibroblasts enhance formation (Fig 4A,C). We are interested in the contribution of fibroblasts to melanoma spheroids so we do not consider the M0:F100 condition in the remainder of the study.

We now explore the quantitative impact of fibroblasts on melanoma spheroid formation time, T [days], using the biphasic model (§3.1) and profile likelihood analysis (§5) to interpret the experimental measurements of spheroid size, $R(t)$ (Fig 4D). For each condition, profile likelihoods for T are well-formed and relatively narrow about a single central peak suggesting T is practically identifiable. Three out of the four profiles appear to be consistent suggesting that spheroid formation time relative to the experimental duration is not drastically altered across the conditions (Fig 4E, Table 1). It is not clear if the profile for M25:F75 is different for a biologically meaningful reason or due to experimental noise (Fig 4E). In Supplementary S4.2 we show that, for each condition, experimental data are accurately described by simulating the biphasic mathematical model with the MLE.

Condition	Formation time, T [days]
M100:F0	1.94 (1.62, 2.04)
M75:F25	1.45 (1.33, 1.66)
M50:F50	1.60 (1.41, 1.81)
M25:F75	2.37 (2.18, 2.60)
M0:F100	1.63 (1.15, 3.13)

Table 1: Estimates of spheroid formation time, T [days] for 1205Lu co-culture spheroids. Results show MLE and 95% approximate confidence intervals.

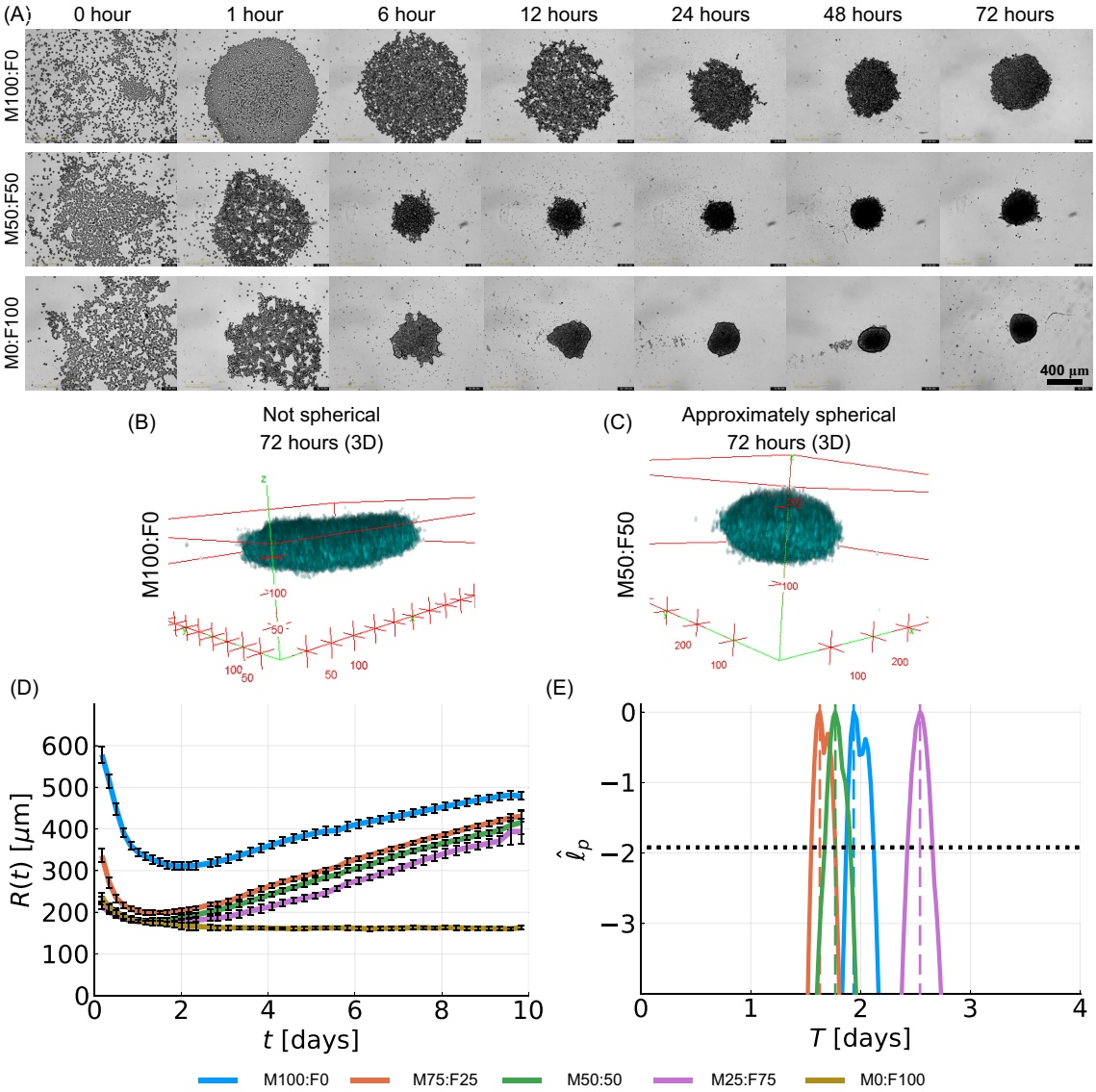

Figure 4: Spheroid formation analysis. Results shown for co-culture spheroids formed with the 1205Lu cell line and fibroblasts. (A) Brightfield experimental images captured from above each spheroid at 0, 1, 6, 24, 48, and 72 [hours]. (B,C) 3D rendering from confocal microscopy z-stack images at 72 hours for (B) M100:F0 and (C) M50:F50 spheroids. The spheroid in (B) is relatively flat while it is reasonable to approximate the spheroid in (C) as spherical. Scale in (B,C) is microns. Colour represents a cell nuclear stain (DAPI) for melanoma cells and fibroblasts. (D) Temporal evolution of measurements of spheroid size, $R(t)$ [µm]. Error bars represent standard deviation about the mean at each time point. (E) Profile likelihoods for formation time, T [days], with approximate 95% confidence interval threshold (horizontal black-dashed). Throughout M100:F0 (blue), M75:F25 (orange), M50:F50 (green), M25:F75 (magenta), and M0:F100 (yellow).

6.2 Temporal evolution of spheroid size

We now focus on co-culture experiments performed using the WM983B melanoma cell line. In contrast to the 1205Lu spheroids, WM983B co-culture spheroids are dense and compact across all conditions (M100:F0, M75:F25, M50:F50, M25:F75) (Fig 5A). The temporal evolution of spheroid size, $R(t)$, is approximately linear in all conditions (Fig 5B). Therefore, we analyse the data using a linear model (Eq (2). Profile likelihoods for $R(3)$ capture that spheroids seeded with a greater proportion of melanoma cells initially form larger spheroids (Fig 5C, Table 2). Profile likelihoods for λ suggest the growth rates are consistent across conditions (Fig 5D, Table 2). Previous monoculture results suggest that increasing the experimental duration results in sigmoidal growth [5, 6, 15].

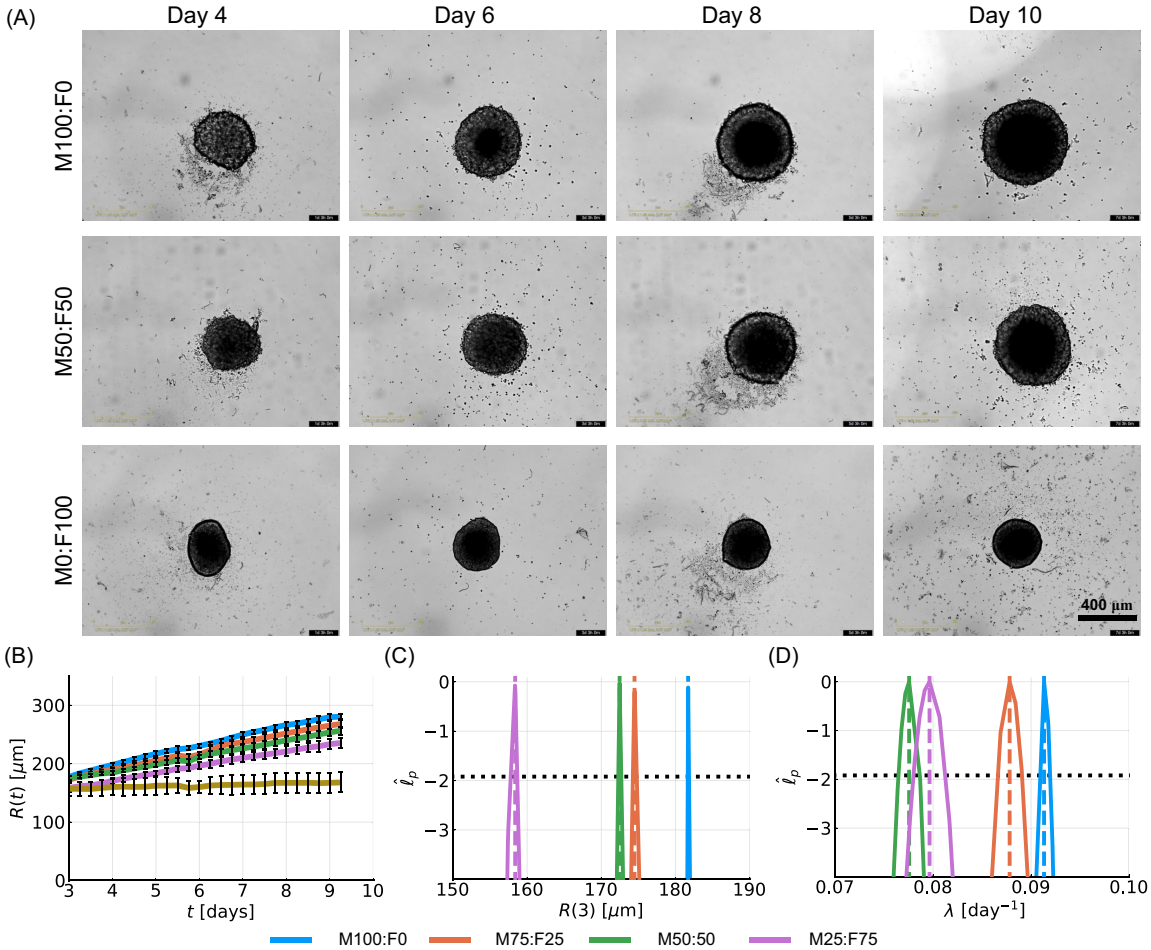

Figure 5: Temporal evolution of spheroid structure. Results shown for co-culture spheroid experiments formed with the WM983B cell line and fibroblasts. (A) Brightfield experimental images captured from above each spheroid. Exemplar image masks shown in Figure 2. (B) Temporal evolution of overall spheroid size $R(t)$ [µm]. (C) Profile likelihoods for initial spheroid size, $R(3)$ [µm]. (D) Profile likelihoods for growth rate, λ [day^{-1}]. In (C,D) approximate 95% confidence interval threshold shown with horizontal black-dashed line. Throughout conditions are M100:F0 (blue), M75:F25 (orange), M50:F50 (green), M25:F75 (magenta), and M0:F100 (yellow).

Condition	Initial Radius, $R(3)$ [µm]	Growth rate, λ [day^{-1}]
M100:F0	181.69 (181.64, 181.82)	0.0913 (0.0909, 0.0920)
M75:F25	174.47 (174.26, 174.80)	0.0878 (0.0866, 0.0891)
M50:F50	172.46 (172.28, 172.70)	0.0776 (0.0765, 0.0786)
M25:F75	158.38 (157.76, 158.66)	0.0796 (0.0780, 0.0812)

Table 2: Estimates of linear model parameters for WM983B co-culture spheroids. Parameters reported include the initial spheroid radius, $R(3)$ [µm], and the growth rate, λ [day^{-1}]. Results show MLE and 95% approximate confidence intervals.

6.3 Temporal evolution of spheroid size and structure

Here we explore the role of fibroblasts on melanoma spheroid size and structure. We analyse confocal microscopy images of each spheroid's equatorial plane, measure $R(t)$ and $R_{\mathrm{n}}(t)$, and interpret these data using a series of mathematical models and profile likelihood analysis.

To identify living and proliferating regions within each spheroid we use FUCCI signals. FUCCI signals indicate different stages of the cell cycle: cells in gap 1 (G1) phase fluoresce red, shown in magenta for clarity; and cells in synthesis, gap 2, and mitotic (S/G2/M) phases fluoresce green (Figure 1I). Now consider the FUCCI signals for M100:F0 spheroids (Fig 6A). On days 2 and 3 magenta and green FUCCI signals are present throughout the spheroid indicating all cells are living and proliferating. From day 6 onwards the large central region without FUCCI signals indicates a necrotic core, previously confirmed by both confocal microscopy and flow cytometry using cell death markers [6, 12, 14, 60]. Outside of the necrotic core FUCCI signals indicate a proliferating region at the periphery (predominately green) and an intermediate region of living cells that are proliferation-inhibited (predominately magenta). We observe similar behaviour, albeit the necrotic core forms later, for M75:F25, M50:F50, and M25:F75 spheroids (Fig 6). Using standard image processing techniques we measure $R(t)$ and $R_{\mathrm{n}}(t)$ (Figs 7A-D, §2, §S1.2). We focus on $R(t)$ and $R_{\mathrm{n}}(t)$ to present results in terms of typical measurements and this means that we group together the proliferating and proliferation-inhibited regions [6].

Seeking to characterise co-culture spheroid growth, we again turn to mathematical modelling and profile likelihood analysis. We consider a reduced version of Greenspan's mathematical model [22], introduced by Burton [34], and focus on the temporal evolution of $R(t)$ and $R_{\mathrm{n}}(t)$ (§4.2). This model is relatively simple. Further, all mechanisms and parameters in the model are biologically interpretable. This is a great advantage over more complicated models where the biological meaning of parameters and mechanisms is not always clear. Note that this mathematical model assumes a monoculture spheroid whereas the experimental data comprise of measurements of co-culture spheroids. We take this approach deliberately. This approach allows us to explore whether estimates of parameters that characterise growth vary across experimental conditions.

For each experimental condition, the monoculture model simulated with the MLE shows excellent agreement with measurements of $R(t)$ and $R_{\mathrm{n}}(t)$ (Figs 7A-D). Profile likelihoods suggest that all model parameters are practically identifiable since the univariate profiles are each well-formed around a single peak (Figs 7E-I, Table 3). The profile for $R(2)$ [µm] suggests the experimental condition influences the initial size of each spheroid (Fig 7E, Table 3). Profiles for the proliferation rate per unit volume of living cells, s [day^{-1}], the dimensionless parameter related to the loss rate from the necrotic core, γ [-], and size of the spheroid when the necrotic region forms, $\mathcal{R}$ [µm], appear to be consistent across all conditions (Fig 7F,G,H, Table 3). Profiles for the standard deviation (Fig 7I, Table 3) capture variability in the experimental data (Fig 7A-D). These powerful quantitative insights suggest that growth characteristics are similar across conditions. Spheroid structure, assessed by measuring

the necrotic fraction, $R_n(t)/R(t)$ [-], also appears to be consistent across conditions (Fig 7J).

Condition	$R(2)$ [µm]	s [day^{-1}]	γ [-]	$\mathcal{R}$ [µm]	σ [µm]
M100:F0	201.2 (197.7, 205.1)	0.247 (0.226, 0.267)	2.00 (1.69, 2.31)	224.6 (220.6, 228.5)	7.5 (5.7,7.8)
M75:F25	181.5 (175.3, 187.9)	0.250 (0.218, 0.283)	2.36 (1.59, 3.13)	223.6 (216.9, 230.2)	12.5 (10.3,14.0)
M50:F50	175.5 (168.5, 182.4)	0.234 (0.202, 0.267)	3.50 (2.09, 4.95)	231.4 (225.6, 237.2)	12.2 (10.5,14.4)
M25:F75	159.6 (155.5, 163.4)	0.212 (0.192, 0.231)	1.94 (0.68, 3.07)	211.6 (208.4, 214.9)	9.1 (7.2,9.8)

Table 3: Estimates of monoculture reduced Greenspan model parameters for WM983B co-culture spheroids. Parameters reported include $R(2)$ [µm], s [day^{-1}], γ [-], $\mathcal{R}$ [µm], and σ [µm]. Results show MLE and 95% approximate confidence intervals.

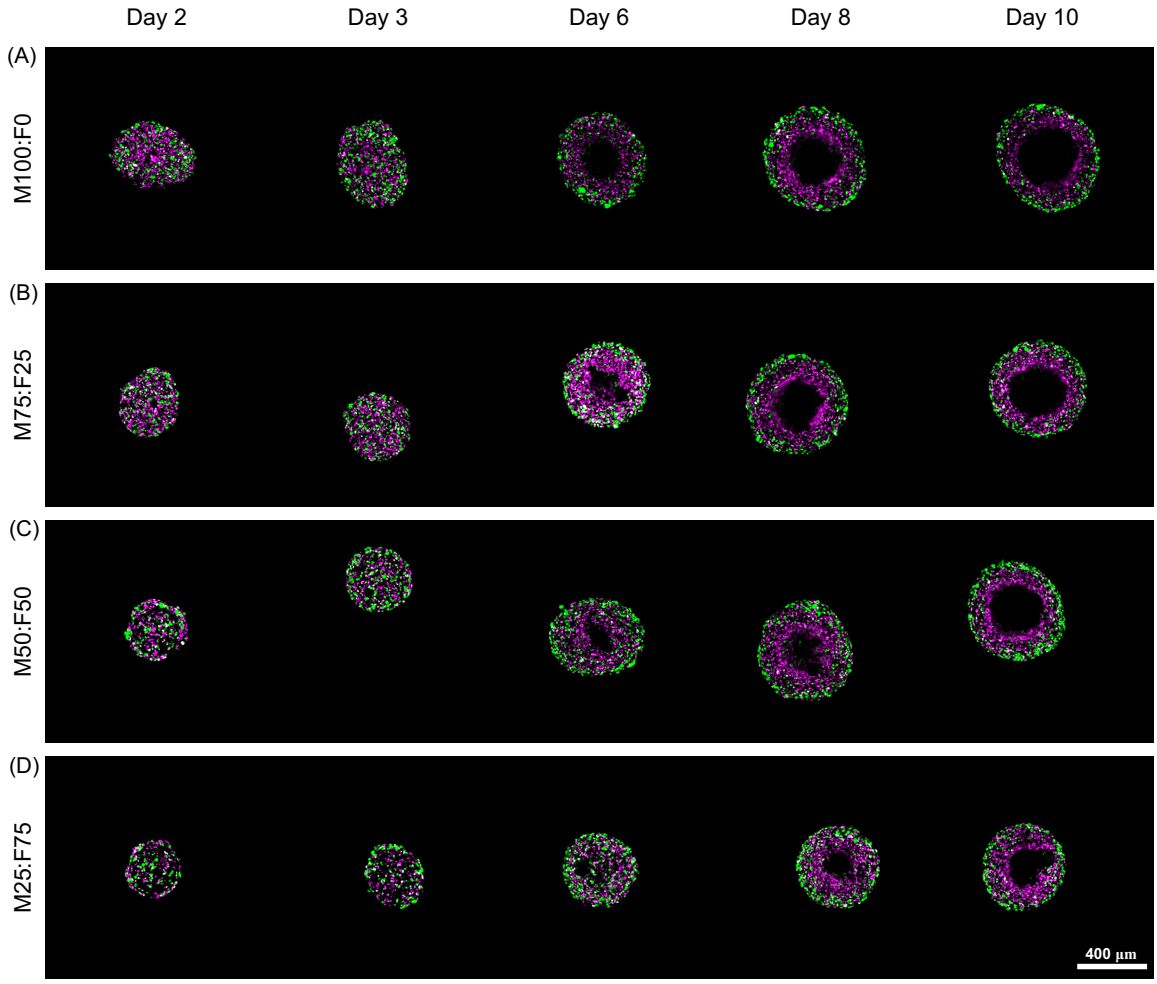

Figure 6: Spatio-temporal evolution of tumour spheroid structure. Confocal microscopy images of each spheroid's equatorial plane for (A) M100:F0, (B) M75:F25, (C) M50:F50, and (D) M25:F75 spheroids. Results shown for the WM983B melanoma cell line. FUCCI signals are shown with magenta and green. Presence of FUCCI signal indicates living cells whereas large regions at the centre of spheroids that lack FUCCI signals indicate a necrotic core. Fibroblasts are not shown so that it is easier to visualise the necrotic core and overall size.

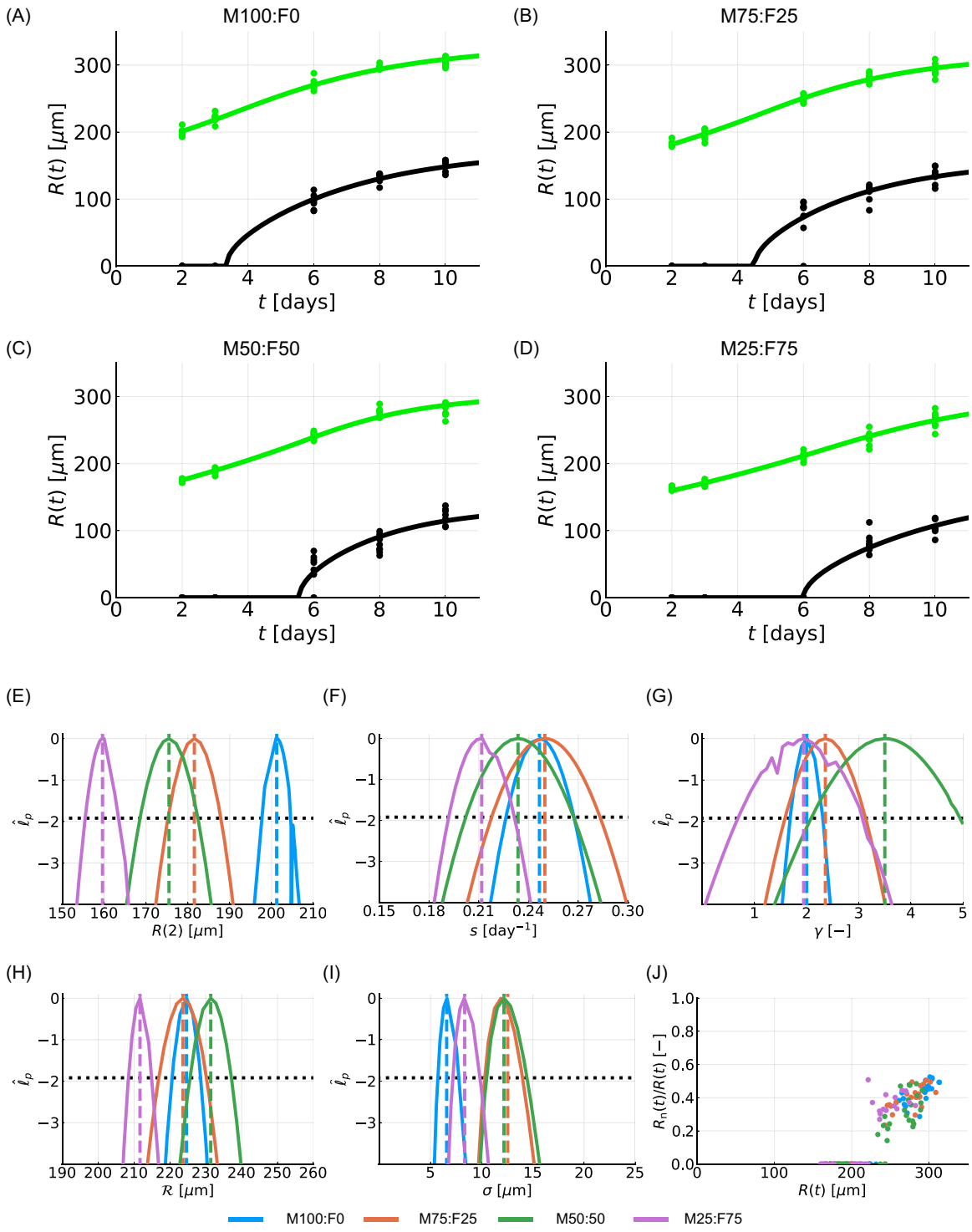

Figure 7: Temporal evolution of spheroid size and structure analysed using the reduced Greenspan mathematical model. (A-D) Comparison of experimental data and mathematical model simulated with the maximum likelihood estimate for: (A) M100:F0; (B) M75:F25; (V) M50:F50; (D) M25:F75 spheroids. In (A-D) experimental measurements of spheroid radius, $R(t)$ [µm], and necrotic radius, $R_{\mathrm{n}}(t)$ [µm], shown as green and black circles, respectively. (E-H) Profile likelihoods for (E) $R(T)$ [µm]; (F) s [day^{-1}]; (G) γ [-]; (H) $\mathcal{R}$ [µm], and (I) σ [µm]. In (E-I) approximate 95% confidence interval threshold shown with horizontal black-dashed line. (J) Measurements of the necrotic fraction, $R_{\mathrm{n}}(t)/R(t)$ [-], against spheroid radius, $R(t)$ [µm]. Throughout conditions are M100:F0 (blue), M75:F25 (orange), M50:F50 (green), and M25:F75 (magenta).

Thus far we have examined the experimental images using FUCCI signals to identify regions of living melanoma cells, that are proliferating or proliferation-inhibited, and necrotic matter. Here, we re-examine these experimental images and include the signal from the fibroblast marker (Fig 8, Supplementary S1.2). Focusing on the M75:F25, M50:F50, and M25:F75 spheroids, fibroblasts are present throughout each spheroid on days 2 and 3 (Fig 8B,C,D). At later times we only observe fibroblasts close to the centre of the spheroid. The biological mechanisms driving the changing position of the fibroblasts within the spheroid are unclear. Seeking further insights we again turn to mathematical modelling and systematically extend the monoculture reduced Greenspan model.

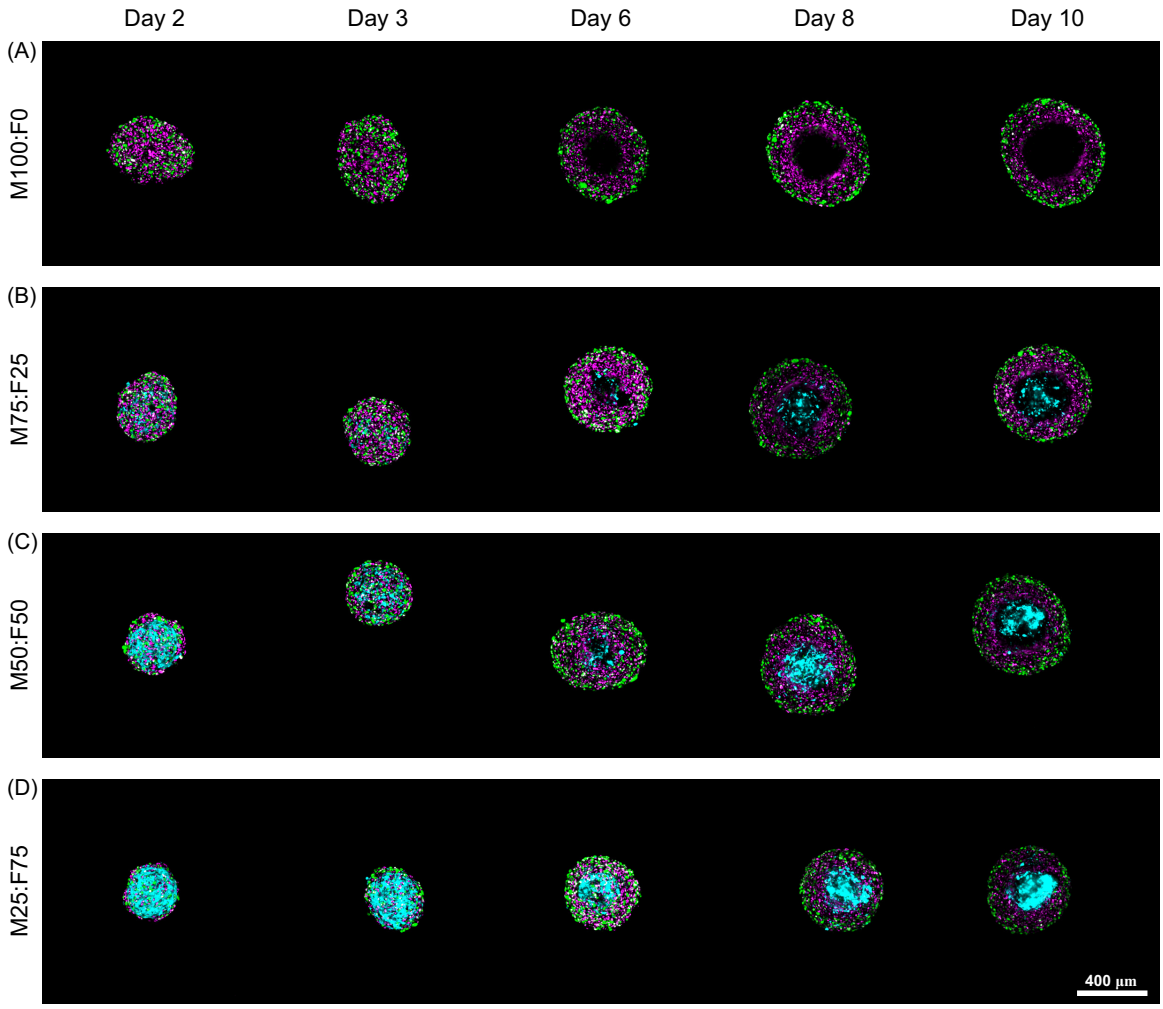

Figure 8: Spatio-temporal evolution of tumour spheroid structure including fibroblast marker. Confocal microscopy images of each spheroid's equatorial plane for (A) M100:F0, (B) M75:F25, (C) M50:F50, and (D) M25:F75 spheroids. These are same spheroids as shown in Fig (6) now with the fibroblast marker shown in cyan. The fibroblast marker stains the entire cell whereas the FUCCI signal is only present at the cell nucleus.

We systematically extend the monoculture model by introducing heterogeneity into s, γ, and $\mathcal{R}$ independently and in turn. This results in four new co-culture models: (i) heterogeneity in s (§4.3); (ii) heterogeneity in γ (§4.4); (iii) heterogeneity in $\mathcal{R}$ (§4.5); and (iv) heterogeneity in $\mathcal{R}$ and an additional cell migration mechanism (§4.6). Parameter values are chosen to capture, where possible, loss of fibroblasts from the periphery and chosen so that model simulations agree with measurements of $R(t)$ and $R_n(t)$ from the M50:F50 condition. Similar results are obtained for M75:F25 and M25:F75 conditions.

In Co-culture Model 1 (§4.3) we assume that melanoma cells and fibroblasts proliferate at different rates per unit volume, s_{m} [day^{-1}] and s_{f} [day^{-1}], respectively (Fig 1I). Simulating Model 1 with $s_{\mathrm{m}} > s_{\mathrm{f}}$ we can capture the temporal evolution of measurements of $R(t)$ and $R_{\mathrm{n}}(t)$ (Fig 9A). For greater insight, we analyse the temporal evolution of the volume of melanoma cells and fibroblasts within each compartment $j = 1, 2$ of the spheroid, denoted $V_{\mathrm{m}}^{(j)}(t)$ and $V_{\mathrm{f}}^{(j)}(t)$, respectively. Here compartment one represents the periphery, $R_{\mathrm{n}}(t) < r < R(t)$, and compartment two represents the necrotic core, $0 < r < R_{\mathrm{n}}(t)$. For each compartment the melanoma fraction is $\phi_{\mathrm{m}}^{(j)}(t) = V_{\mathrm{m}}^{(j)}(t)/[V_{\mathrm{m}}^{(j)}(t) + V_{\mathrm{f}}^{(j)}(t)]$. Since $\phi_{\mathrm{m}}^{(1)}(t) \to 1$ as $t \to \infty$, Co-culture Model 1 captures the loss of fibroblasts from the periphery (Fig 9B). Further, since $\phi_{\mathrm{m}}^{(2)}(t) \to 1$ as $t \to \infty$, Co-culture Model 1 suggests that the necrotic core will eventually be composed only of matter from necrotic melanoma cells (Fig 9B). This is a useful insight. In experimental images we are unable to quantify the proportion of necrotic matter that is from melanoma cells and fibroblasts due to loss of signal during necrosis.

In Co-culture Model 2 (§4.4), we assume that the rate at which mass in the necrotic core degrades and is lost from the spheroid depends on whether the necrotic matter is from melanoma cells or fibroblasts (Fig 1J). This is associated with two parameters γ_{m} [-] and γ_{f} [-]. Simulating Co-culture Model 2 we can capture the temporal evolution of measurements of $R(t)$ and $R_{\mathrm{n}}(t)$ but we cannot capture the loss of fibroblasts at the periphery (Fig 9C,D).

In Co-culture Models 3 (§4.5) and 4 (§4.6), we generalise the single oxygen partial pressure threshold, p_{n} [%], with two thresholds, $p_{\mathrm{f}} \geq p_{\mathrm{m}}$ [%], corresponding to the oxygen partial pressure below which fibroblasts and melanoma cells die, respectively (Fig 1K,L). These two thresholds define $R_{\mathrm{f}}(t)$ and $R_{\mathrm{m}}(t)$, respectively, that satisfy $R_{\mathrm{f}}(t) \geq R_{\mathrm{m}}(t)$ (Fig 1N), and two parameters ($\mathcal{R}_{\mathrm{f}}$, $\mathcal{R}_{\mathrm{m}}$). This gives rise to a model with three compartments (Fig 1I-N). Here we assume that measurements of the necrotic core correspond to measurements of $R_{\mathrm{m}}(t)$ that is defined by p_{m}. This is because we measure the size of the necrotic region using FUCCI signals from melanoma cells. Similarly to Co-culture Model 2, with Co-culture Model 3 we can capture the temporal evolution of measurements of $R(t)$ and $R_{\mathrm{m}}(t)$ (Fig 9E) but cannot capture the loss of fibroblasts at the periphery (Fig 9F).

Introducing additional cell migration into Co-culture Model 3 gives Co-culture Model 4. We assume that living fibroblasts at the periphery, $R_{\mathrm{f}}(t) \leq r \leq R(t)$, migrate towards the centre of the spheroid, $R_{\mathrm{m}}(t) \leq r \leq R_{\mathrm{f}}(t)$, while the same volume of melanoma cells migrate in the opposite direction (Fig 1N). This can give rise to transient dynamics where the proportion of fibroblasts at the core increases followed by long-term loss of fibroblasts throughout the spheroid (Fig 9G,H). There

are many biological reasons why this migration could occur and this model does not rule in or out any possibility. Experimental observations for co-culture spheroids with the 1205Lu cell line suggest that fibroblasts can form the core of spheroids at earlier times (Supplementary S4.4).

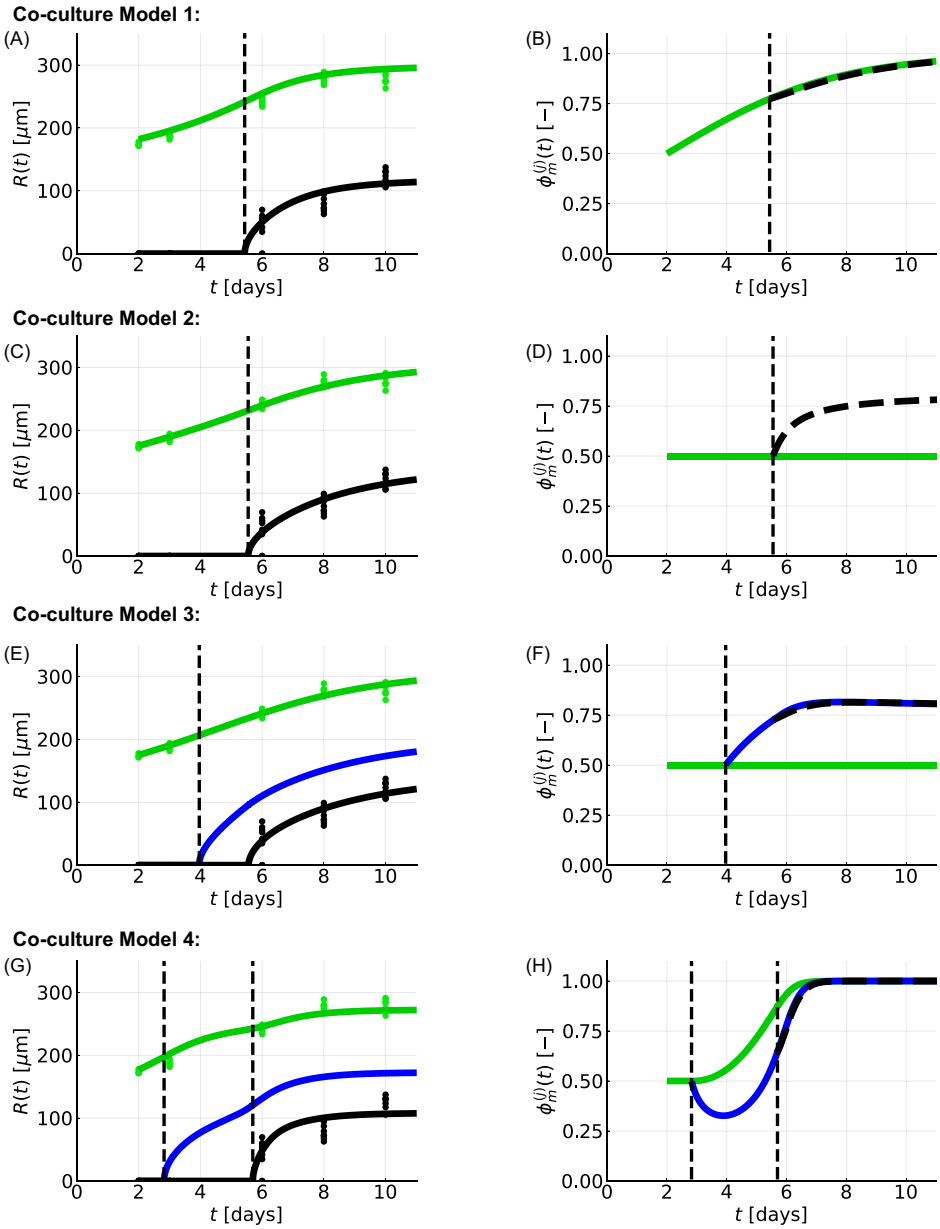

Figure 9: Spatio-temporal evolution of spheroid structure analysed using multiple co-culture reduced Greenspan models. (A,C,E,G) Simulations of (A) Co-culture Model 1, (C) Co-culture Model 2, (E) Co-culture Model 3, (G) Co-culture Model 4 show the temporal evolution of spheroid size $R(t)$ (green). For Co-culture Models 1 and 2 we present the size of necrotic core $R_{\mathrm{n}}(t)$ (black). For Co-culture Models 3 and 4 we present $R_{\mathrm{f}}(t)$ (blue) and $R_{\mathrm{m}}(t)$ (black). Experimental measurements of $R(t)$ and necrotic core from M50:F50 spheroids are shown as green and black circles, respectively. (B,D,F,H) Temporal evolution of melanoma fraction $\phi_{\mathrm{m}}^{(j)}(t) = V_{\mathrm{m}}^{(j)}(t)/[V_{\mathrm{m}}^{(j)}(t) + V_{\mathrm{f}}^{(j)}(t)]$ for regions $j = 1$ (green), 2 (black dashed) in Co-culture Models 1 and 2, and $j = 1$ (green), 2 (black dashed), 3 (blue) in Models 3 and 4. Parameters used: Co-culture Model 1, $(R(T), V_{\mathrm{m}}(T), s_{\mathrm{m}}, s_{\mathrm{f}}, \gamma, \mathcal{R}) = (177, 0.5(4\pi/3)177^3, 0.35, 0.1, 3.07, 235)$; Co-culture Model 2, $(R(T), V_{\mathrm{m}}(T), s, \gamma_{\mathrm{m}}, \gamma_{\mathrm{f}}, \mathcal{R}) = (175.35, 0.5(4\pi/3)175.35^3, 0.235, 2.07, 8.00, 231.44)$; Co-culture Model 3, $(R(T), V_{\mathrm{m}}(T), s, \gamma, \mathcal{R}_{\mathrm{m}}, \mathcal{R}_{\mathrm{f}}) = (176.00, 0.5(4\pi/3)176.00^3, 0.244, 2.060, 207.07, 220.94)$; and Co-culture Model 4, $(R(T), V_{\mathrm{m}}(T), s, \gamma, \mathcal{R}_{\mathrm{m}}, \mathcal{R}_{\mathrm{f}}, \omega) = (177.0, 0.5(4\pi/3)177^3, 0.4, 5.00, 197.5, 220.0, 9.75 \times 10^{-7})$.

7 Conclusion

In this study we develop a general mathematical and statistical framework to characterise and interpret co-culture spheroid formation and growth. The work includes novel theoretical and biological contributions. We perform a series of co-culture spheroid experiments and use our mathematical and statistical modelling framework to quantify spheroid formation time and estimate key parameters that characterise growth. We find that in our experiments introducing a second cell type allows a cancer cell line to generate spheroids with approximately spherical structures that would not otherwise. Further, we find that the second cell type has limited impact on formation time, spheroid growth and structure. There are many possible reasons for these results. For example it could be that there are limited interactions, or cross-talk, between the melanoma cells and fibroblasts. As part of this analysis we quantitatively directly connect a version Greenspan's seminal model to co-culture spheroid data for the first time. We choose to use a monoculture model to describe co-culture data deliberately. This approach allows us to explore whether estimates of parameters that characterise growth vary across experimental conditions and we find this to be insightful. In addition, by extending a general class of monoculture compartment-based mathematical models to multiple populations, we reveal biological mechanisms that can describe the internal dynamics of co-culture spheroids and those that cannot. This framework is important because there is, at present, no widely used and commonly accepted framework for modelling and interpreting co-culture spheroid growth where nutrient limitations and geometric constraints play a role in constraining spheroid growth.

Our mathematical and statistical modelling framework can be applied to different cell types and to spheroids grown in different conditions. Here we choose to perform experiments with melanoma cells and fibroblasts. This builds on our previous monoculture melanoma spheroid studies [5, 6, 15, 14]. Our results are consistent with analysis of two-dimensional experiments which suggest that fibroblasts have a limited impact on co-culture melanoma spreading and invasion [61]. However, we note that other spheroid studies suggest fibroblasts contribute to melanoma spheroid growth [11]. Interesting future work would be to explore these differences. Such differences could arise due to many reasons, for example choice of cell line, fibroblasts, and experimental conditions. Further, the framework is well-suited to diagnose cross-talk in other co-culture experiments.

In our WM983B co-culture experiments fibroblasts are present throughout the spheroid at early times but are only present in the central region of the spheroid at later times [10, 33]. Using our new mathematical models we identify that differences in proliferation rates, or differences in when each cell undergoes necrosis due to lack of oxygen in combination with cell migration, could drive this behaviour. Performing additional experiments to inhibit proliferation or growing co-culture spheroids in different oxygen conditions may be insightful [15]. In general, additional data would be helpful to assess whether parameter identifiability in the co-culture mathematical models. Our framework is well-suited to incorporate such additional data and, if appropriate, different error models [19].

The co-culture mathematical modelling framework is general. We use this framework to extend

the monoculture reduced Greenspan mathematical model to two populations. This allows us to explore the temporal evolution of co-culture spheroid size and structure. In §S4.1 we present further examples of the general model, including the seminal Greenspan model and the radial-death model [18]. The radial-death model captures key features of Greenspan's model, but rather than considering oxygen mechanisms prescribes a fixed size for the proliferating region. Many other models could be considered with additional compartments and/or mechanisms such as nutrient/waste diffusion and consumption/production. For example, we could use our experimental images to identify regions where melanoma cells are proliferation-inhibited and incorporate this into mathematical modelling [5, 6, 15, 22]. In general, the additional complexity of these models may result in parameter identifiability challenges with currently available data [18, 20]. Incorporating mechanical effects is also of interest [62, 63]. The framework could also be extended to characterise the effectiveness of chemotherapies and radiotherapies [8, 9, 10, 11, 64, 65]. Overall, this study lays a theoretical foundation to characterise co-culture tumour spheroid formation and growth.

Code and data availability

Key computer code used to generate computational results and datasets generated and analysed during this study are summarised in the electronic supplementary material and are available on a GitHub repository (https://github.com/ryanmurphy42/Murphy2022CoCulture).

Author's contributions

All authors conceived and designed the study. RJM performed the mathematical and statistical modelling, and drafted the article. GG performed all experimental work. All authors provided comments and approved the final version of the manuscript. NKH and MJS contributed equally.

Competing interests

We declare we have no competing interest.

Funding

MJS and NKH are supported by the Australian Research Council (DP200100177).

Acknowledgements

We thank Associate Professor Rick Sturm, Frazer Institute (University of Queensland) for providing the fibroblasts. We thank John Blake for guidance using IncuCyte. This research was carried out at the Translational Research Institute (TRI), Woolloongabba, QLD. TRI is supported by a grant from the Australian Government. We thank the staff in the microscopy core facility at TRI for their technical support. We thank Professor Atsushi Miyawaki, RIKEN, Wako-city, Japan, for providing the FUCCI constructs, and Professor Meenhard Herlyn, The Wistar Institute, Philadelphia, PA, for providing the cell lines.

References

[1] Costa EC, Moreira AF, de Melo-Diogo D, Gaspar VM, Carvalho MP, Correia IJ. 2016. 3D tumor spheroids: An overview on the tools and techniques used for their analysis. Biotechnology Advances. 34, 1427-1441. (doi:10.1016/j.biotechadv.2016.11.002)

[2] Hirschhaeuser F, Menne H, Dittfled C, West J, Mueller-Klieser W, Kunz-Schughart LA. 2010. Multicellular tumor spheroids: An underestimated tool is catching up again. Journal of Biotechnology. 148, 3-15. (doi:10.1016/j.jbiotec.2010.01.012)

[3] Mehta G, Hsiao AY, Ingram M, Luker GD, Takayama S. 2012. Opportunities and challenges for use of tumor spheroids as models to test drug delivery and efficacy. Journal of Controlled Release. 10, 192-204. (doi:10.1016/j.jconrel.2012.04.045)

[4] Beaumont KA, Mohana-Kumaran N, Haass NK. 2014. Modeling Melanoma In Vitro and In Vivo. Healthcare. 2, 27-46. (doi:10.3390/healthcare2010027)

[5] Browning AP, Sharp JA, Murphy RJ, Gunasingh G, Lawson B, Burrage K, Haass NK, Simpson MJ. 2021. Quantitative analysis of tumour spheroid structure. eLife. 10, e73020. (doi:10.7554/eLife.73020)

[6] Murphy RJ, Browning AP, Gunasingh G, Haass NK, Simpson MJ. 2022. Designing and interpreting 4D tumour spheroid experiments. Communications Biology. 5, 91. (doi:10.1038/s42003-022-03018-3)

[7] Murphy RJ, Gunasingh G, Haass NK, Simpson MJ. 2023. Growth and adaptation mechanisms of tumour spheroids with time-dependent oxygen availability. PLoS Computational Biology. 19, e1010833 (doi:10.1371/journal.pcbi.1010833)

[8] Tofilon PJ, Buckley N, Deen DF. 1984. Effect of cell-cell interactions on drug sensitivity and growth of drug-sensitive and-resistant tumor cells in spheroids. Science. 226, 862-864. (doi:10.1126/science.6494917)

[9] Paczkowski M, Kretzschmar WW, Markelc B, Liu SK, Kunz-Schughart LA, Harris AL, Partridge M, Byrne HM, Kannan P. 2021. Reciprocal interactions between tumour cell populations enhance growth and reduce radiation sensitivity in prostate cancer. Communications Biology. 4, 6. (doi:10.1038/s42003-020-01529-5)

[10] Yakavets I, Francois A, Benoit A, Merlin J-L, Bezdetnaya L, Vogin G. 2020. Advanced co-culture 3D breast cancer model for investigation of fibrosis induced by external stimuli: optimization study. Scientific Reports. 10, 21273. (doi:10.1038/s41598-020-78087-7)

[11] Flach EH, Rebecca VW, Herlyn M, Smalley KS, Anderson AR. 2011. Fibroblasts contribute to melanoma tumor growth and drug resistance. Molecular Pharmaceutics. 8, 2039-2049. (doi:10.1021/mp200421k)

[12] Spoerri L, Gunasingh G, Haass NK. 2021. Fluorescence-based quantitative and spatial analysis of tumour spheroids: a proposed tool to predict patient-specific therapy response. Frontiers in Digital Health. 3, 668390. (doi:10.3389/fdgth.2021.668390)

[13] Spoerri L, Beaumont KA, Anfosso A, Haass NK. 2017. Real-time cell cycle imaging in a 3D cell culture model of melanoma. Methods in Molecular Biology. 1612, 401–416. (doi:10.1007/978-1-4939-7021-6_29)

[14] Haass NK, Beaumont KA, Hill DS, Anfosso A, Mrass P, Munoz MA, Kinjyo I, Weninger W. 2014. Real-time cell cycle imaging during melanoma growth, invasion, and drug response. Pigment Cell & Melanoma Research. 27, 764-76. (doi:10.1111/pcmr.12274)

[15] Murphy RJ, Maclaren OJ, Calabrese AR, Thomas PB, Warne DJ, Williams ED, Simpson MJ. 2022. Computationally efficient framework for diagnosing, understanding, and predicting biphasic population growth. Journal of the Royal Society Interface. 19, 20220560 (doi:10.1098/rsif.2022.0560)

[16] Gerlee P. 2013. The model muddle: In search of tumor growth laws. Cancer Research. 73, 2407-2411. (doi:10.1158/0008-5472.CAN-12-4355)

[17] Sarapata EA, de Pillis LG. 2014. A comparison and catalog of intrinsic tumor growth models. Bulletin of Mathematical Biology. 76, 2010-2024. (doi:10.1007/s11538-014-9986-y)

[18] Browning AP, Simpson MJ. 2023. Geometric analysis enables biological insight from complex non-identifiable models using simple surrogates. PLoS Computational Biology. 19, e1010844. (doi:10.1371/journal.pcbi.1010844)

[19] Pawitan Y. 2001. In All Likelihood: Statistical Modelling And Inference Using Likelihood. Oxford, UK: Oxford University Press.

[20] Simpson MJ, Baker RE, Vittadello ST, Maclaren OJ. 2020. Practical parameter identifiability for spatio-temporal models of cell invasion. Journal of the Royal Society Interface. 17, 2020055. (doi:10.1098/rsif.2020.0055)

[21] Raue A, Kreutz C, Maiwald T, Bachmann J, Schilling M, Klingmüller U, Timmer J. 2009. Structural and practical identifiability analysis of partially observed dynamical models by exploiting the profile likelihood. Bioinformatics. 25, 1923-1929. (doi:10.1093/bioinformatics/btp358).

[22] Greenspan HP. 1972. Models for the growth of a solid tumor by diffusion. Studies in Applied Mathematics. 51, 317-340. (doi:10.1002/sapm1972514317)

[23] Sakaue-Sawano A, Kurokawa H, Morimura T, Hanyu A, Hama H, Osawa H, Kashiwagi S, Fukami K, Miyata T, Miyoshi H, et al. 2008. Visualizing spatiotemporal dynamics of multicellular cell-cycle progression. Cell. 132, 487-98. (doi:10.1016/j.cell.2007.12.033)

[24] Araujo RP, McElwain DLS. 2004. A history of the study of solid tumour growth: the contribution of mathematical modelling. Bulletin of Mathematical Biology. 66, 1039-1091. (doi:10.1016/j.bulm.2003.11.002)

[25] Bull JA, Byrne HM. 2022. The hallmarks of mathematical oncology. Proceedings of the IEEE. 110, 523-540. (doi:10.1109/JPROC.2021.3136715)

[26] Byrne HM. 2010. Dissecting cancer through mathematics: from the cell to the animal model. Nature Reviews Cancer. 10, 221-30. (doi:10.1038/nrc2808)

[27] Lowengrub JS, Friebos HB, Jin F, Chuang Y-L, Li X, Macklin P, Wise SM, Cristini V. 2010. Nonlinear modelling of cancer bridging the gap between cells and tumours. Nonlinearity. 23, 1-91. (doi:10.1088/0951-7715/23/1/R01)

[28] Bull JA, Mech F, Quasier T, Waters SL, Byrne HM. 2020. Mathematical modelling reveals cellular dynamics within tumour spheroids. PLoS Computational Biology. 16, e1007961. (doi:10.1371/journal.pcbi.1007961)

[29] Klowss JJ, Browning AP, Murphy RJ, Carr EJ, Plank MJ, Gunasingh G, Haass NK, Simpson MJ. 2022. A stochastic mathematical model of 4D tumour spheroids with real-time fluorescent cell cycle labelling. Journal of the Royal Society Interface. 19, 20210903. doi:10.1098/rsif.2021.0903

[30] Jagiella N, Müller B, Müller M, Vignon-Clementel IE, Drasdo D. 2016. Inferring growth control mechanisms in growing multi-cellular spheroids of NSCLC cells from spatial-temporal image data. PLoS Computational Biology. 12, e1004412. (doi:10.1371/journal.pcbi.1004412)

[31] Ward JP, King JR. 1997. Mathematical modelling of avascular-tumour growth II: modelling growth saturation. Mathematical Medicine and Biology: A Journal of the IMA. 16, 171-211. (doi:10.1093/imammb/16.2.171)

[32] Jin W, Spoerri L, Haass NK, Simpson MJ. 2021. Mathematical model of tumour spheroid experiments with real-time cell cycle imaging. Bulletin of Mathematical Biology. 83, 1-23. (doi:10.1007/s11538-021-00878-4)

[33] Fang G, Lu H, Law A, Gallego-Ortega D, Jin D, Lin G. 2019. Gradient-sized control of tumor spheroids on a single chip. Lab on a Chip. 19, 4093-4103. (doi:10.1039/C9LC00872A)

[34] Burton AC. 1966. Rate of growth of solid tumours as problem of diffusion. Growth. 30, 157-176.

[35] Britton NF. 2003. Essential Mathematical Biology. London, UK: Springer.

[36] Deakin AS. 1975. Model for the growth of a solid in vitro tumour. Growth. 39, 159–165.

[37] McElwain DLS, Ponzo PJ. 1977. A model for the growth of a solid tumor with non-uniform oxygen consumption. Mathematical Biosciences. 35, 267–279. (doi:10.1016/0025-5564(77)90028-1)

[38] McElwain DLS, Morris LE. 1978. Apoptosis as a volume loss mechanism in mathematical models of solid tumor growth. Mathematical Biosciences. 39, 147-157. (doi:10.1016/0025-5564(78)90033-0)

[39] Adam JA. 1986. A simplified mathematical model of tumor growth. Mathematical Biosciences. 81, 229–244. (doi:10.1016/0025-5564(86)90119-7)

[40] Adam JA. 1987. A mathematical model of tumor growth. II. Effects of geometry and spatial uniformity on stability. Mathematical Biosciences. 86, 183–211. (doi:10.1016/0025-5564(87)90010-1)

[41] Adam JA. 1987. A mathematical model of tumor growth. III. Comparison with experiment. Mathematical Biosciences. 86, 213-227 (doi:10.1016/0025-5564(87)90011-3)

[42] Adam JA, Maggelakis SA. 1989. Mathematical models of tumor growth. IV. Effects of a necrotic core. Mathematical Biosciences. 97, 121–136. (doi:10.1016/0025-5564(89)90045-x)

[43] Adam JA, Maggelakis SA. 1990. Diffusion regulated characteristics of a spherical prevascular carcinoma. Bulletin of Mathematical Biology. 52, 549–582. (doi:10.1007/BF02462267)

[44] Maggelakis SA, Adam JA. 1990. Mathematical model of prevascular growth of a spherical carcinoma. Mathematical and Computer Modelling. 13, 23–38. (doi:10.1016/0895-7177(90)90040-T)

[45] Landry J, Freyer JP, Sutherland RM. 1982. A model for the growth of multicellular spheroids. Cell and Tissue Kinetics. 15, 585–594. (doi:10.1111/j.1365-2184.1982.tb01065.x)

[46] Byrne HM, Chaplain MAJ. 1996. Growth of necrotic tumors in the presence and absence of inhibitors. Mathematical Biosciences. 135, 187-216. (doi:10.1016/0025-5564(96)00023-5)

[47] Byrne HM, Chaplain MAJ. 1997. Free boundary problems associated with the growth and development of multicellular spheroids. European Journal of Applied Mathematics. 8, 639-658. (doi:10.1017/S0956792597003264)

[48] Hsu MY, Elder DE, Herylyn M. 2002. Melanoma: the Wistar melanoma (WM) cell lines.

[49] Hoek KS, Schlegel NC, Brafford P, Sucker A, Ugurel S, Kumar R, Weber BL, Nathanson KL, Phillips DJ, Herlyn M, Schadendorf D, Dummer R. 2006. Metastatic potential of melanomas defined by specific gene expression profiles with no BRAF signature Pigment Cell Research. 19, 290–302. (doi:10.1111/j.1600-0749.2006.00322.x.)

[50] Smalley KSM, Contractor R, Haass NK, Kulp AN, Atilla-Gokcumen GE, Williams DS, Bregman H, Flaherty KT, Soengas MS, Meggers E, Meenhard Herlyn. 2007. An organometallic protein kinase inhibitor pharmacologically activates p53 and induces apoptosis in human melanoma cells. Cancer Research. 67, 209–217. (doi:10.1158/0008-5472.CAN-06-1538)

[51] Smalley KSM, Contractor R, Haass NK, Lee JT, Nathanson KL, Medina CD, Flaherty KT, Herlyn M. 2007. Ki67 expression levels are a better marker of reduced melanoma growth following MEK inhibitor treatment than phospho-ERK levels. British Journal of Cancer. 96, 445–449. (doi:10.1038/sj.bjc.6603596)

[52] Ainger SA, Yong XLH, Soyer HP, Sturm RA. 2017. Testing of the viable human skin cell dilution cultures as an approach to validating microsampling. Archives of Dermatological Research. 309, 305-310. (doi:10.1007/s00403-017-1726-3)

[53] McQuin C, Goodman A, Chernyshev V, Kamentsky L, Cimini BA, Karhohs KW, Doan M, Ding L, Rafelski SM, Thirstrup D, Wiegraebe W. 2018. CellProfiler 3.0: Next-generation image processing for biology. PLoS Biology. 16, e2005970. (doi:10.1371/journal.pbio.2005970)

[54] Browning AP, Murphy RJ. 2021. Image processing algorithm to identify structure of tumour spheroids with cell cycle labelling. Zenodo. (doi:10.5281/zenodo.5121093)

[55] Gunasingh G, Browning AP, Haass NK. 2022. Rapid optical clearing for semi-high-throughput analysis of tumour spheroids. Journal of Visualized Experiments. 186, e64103. (doi:10.3791/64103)

[56] Grimes DR, Kelly C, Bloch K, Partridge M. 2014. A method for estimating the oxygen consumption rate in multicellular tumour spheroids. Journal of the Royal Society Interface. 11, 20131124. (doi:10.1098/rsif.2013.1124)

[57] Browning AP, McCue SW, Simpson MJ. 2017. A Bayesian computational approach to explore the optimal duration of a cell proliferation assay. Bulletin of Mathematical Biology. 79, 1888-1906 (doi: 10.1007/s11538-017-0311-4)

[58] Royston P. 2007. Profile likelihood for estimation and confidence intervals. Stata J. 7, 376–387. (doi:10.1177/1536867X0700700305)

[59] Johnson SG. 2022. The NLopt module for Julia. Retrieved 11-Dec-2022 NLopt.

[60] Spoerri L, Tonnessen-Murray CA, Gunasingh G, Hill DS, Beaumont KA, Jurek RJ, Chauhan J, Vanwalleghem GC, Fane ME, Daignault-Mill SM, et al. 2021. Phenotypic melanoma heterogeneity is regulated through cell-matrix interaction dependent changes in tumor microarchitecture. Preprint on bioRxiv. (doi:10.1101/2020.06.09.141747)

[61] Haridas P, Penington CJ, McGovern JA, McElwain DLS, Simpson MJ. 2017. Quantifying rates of cell migration and cell proliferation in co-culture barrier assays reveals how skin and melanoma cells interact during melanoma spreading and invasion. Journal of Theoretical Biology. 423, 13-25. (doi:10.1016/j.jtbi.2017.04.017)

[62] Loessner D, Flegg JA, Byrne HM, Clements JA, Hutmacher DW. 2013. Growth of confined cancer spheroids: a combined experimental and mathematical modelling approach. Integrative Biology. 5, 597-605. (doi:10.1039/c3ib20252f)

[63] Walker BJ, Celora GL, Goriely A, Moulton DE, Byrne HM. 2022. Towards a minimal admissible model of solid tumour spheroid growth. Preprint on arXiv. (doi:10.48550/arXiv.2206.13818)

[64] Lewin TD, Maini PK, Moros EG, Enderling H, Byrne HM. 2018. The evolution of tumour composition during fractionated radiotherapy: implications for outcome. Bulletin of Mathematical Biology. 80, 1207-1235. (doi:10.1007/s11538-018-0391-9)

[65] Nasim A, Yates J, Derks G. Dunlop C. 2022. A spatially resolved mechanistic growth law for cancer drug development predicting tumour growing fractions. Cancer Research Communications. 2, 754-761. (doi:10.1158/2767-9764.CRC-22-0032)